Arabian Journal for Science and Engineering
https://doi.org/10.1007/s13369-024-08979-7

RESEARCH ARTICLE-CIVIL ENGINEERING

From Material to Field Test: An Improved Under Sleeper Pad Model

Arif Ulu[1] · Muzaffer Metin[2] · Aytac Arikoglu[3] · Ozgur Demir[4]

Received: 29 November 2023 / Accepted: 11 March 2024
© The Author(s) 2024

Abstract
This study aims to determine the stiffness values of under sleeper pad (USP) and rail pad (RP) components to reduce the high-amplitude vibrations that occur in the transition zones of some specific structures such as viaducts in ballasted railways. The conventional method of simulating USPs and RPs as spring–dashpot elements in the Kelvin–Voigt model is inadequate due to the absence of frequency and temperature dependencies in the model. The study proposes a new analytical model that considers USPs and RPs as viscoelastic (VE) materials and integrates them into the ballasted railway superstructure model by adding unit masses avoiding mathematical singularity. The process includes material testing, field measurements, and validation of the proposed model with finite element model analysis. The effect of ambient temperature and material modelling on the superstructure's dynamic response in the frequency domain is analysed in detail. To account for VE behaviours of the resilient elements, the generalised Maxwell model (GMM) is chosen via unit mass implementation compared to other VE models. The obtained results show that the dynamic response of the railway superstructure is 8–10 times sensitive to temperature variation. This demonstrates how important it is to include the temperature-dependent dynamics of the elastomer material in the model. According to the other results that were obtained, the use of USP in transition zones does not solve the vibration problem radically. Bridge dynamic responses are also sensitive to the mass of the bridge rather than its stiffness.

Keywords Railway · Viscoelastic · Under sleeper pad · USP · Unit mass model · Transition zone · Generalised Maxwell model · Kelvin–Voigt · DMA

1 Introduction

Transition zones are areas where two different superstructures, such as endings of tunnels and bridges, meet. Due to the merging of two different railway forms, a sudden variation in support stiffness is experienced. Problems like differential track settlement, the irregular geometry of rails, and lack of sleeper support are caused by this imbalance in flexibility [1–3]. In these transition zones, railway dynamic loads are amplified substantially and can result in corruptions in the ballast and the subgrade. As a result, the maintenance and repair of superstructure demand more time and resources from the company's budget [4]. Novel practices for the solution to this problem can be found in the literature involving components such as prefabricated reinforced concrete slabs [5] and under sleeper pads [6–8].

Additionally, studies [9–12] have delved into the dynamic behaviour of railway tracks and the impact of various factors on track deformation, wheel–rail contact forces, and passenger comfort. These studies have highlighted the importance of considering vehicle speed, variations in support stiffness, and different track types in the design and maintenance of railway tracks. Other studies have [13–15] investigated the root causes of issues in transition zones such as differential movement and settlement near bridge abutments. They have offered insights into the mechanisms behind these problems

✉ Aytac Arikoglu
arikoglu@itu.edu.tr

Arif Ulu
arifulu@aydin.edu.tr

Muzaffer Metin
mmetin@yildiz.edu.tr

Ozgur Demir
ozgurd@yildiz.edu.tr

1 Department of Mechanical Engineering, Istanbul Aydin University, Istanbul, Turkey

2 Department of Mechanical Engineering, Yildiz Technical University, Istanbul, Turkey

3 Department of Aeronautical Engineering, Istanbul Technical University, Istanbul, Turkey

4 Department of Naval Architecture and Marine Engineering, Yildiz Technical University, Istanbul, Turkey

Published online: 18 April 2024

and methods to measure and address them effectively. Furthermore, the application of numerical simulations [9, 13, 16–19] and experimental testing [20–22] plays a pivotal role in understanding and optimising railway track behaviours. These approaches enable researchers to model and test various scenarios, improving our ability to design and maintain tracks that meet safety, comfort, and operational criteria.

The use of under sleeper pads (USPs) is a common theme in several studies [6, 7, 10, 14, 23, 24]. USPs were shown to have a positive impact in terms of reducing vertical acceleration, the displacement of sleepers, wheel–rail contact forces, and rail bending stresses [25, 26]. Additionally, when one side of the track is relatively soft (e.g. open track) compared to the other side (e.g. bridge), they are useful in decreasing the stiffness gradient. These findings demonstrate the potential of USPs in enhancing track performance and passenger comfort. The consideration of viscoelastic properties [27, 28] in elastomer elements is a forward-looking approach that seeks to improve the modelling and design of tracks. Fractional calculus and genetic algorithms are employed to identify parameters and develop more accurate models for these materials.

While USPs have demonstrated their potential to enhance railway track performance, there are several unresolved concerns and areas that require further attention to fully harness their advantages. These are the key issues or challenges that still need to be addressed in relation to USPs in railway track systems:

- *Long-Term Resilience* A significant concern revolves around the long-term durability of USPs. They may deteriorate or lose their effectiveness over time due to environmental factors such as moisture, temperature fluctuations, and exposure to UV rays. For example, in a previous study [29], the effect of temperature fluctuations on the sleeper was analysed, whereas its effect on the USP was not. As elastomer-based elements, they are affected by temperature changes in the environment, UV rays, and loads passing over them, and their lifetime varies. Additionally, variations exist between the products of different manufacturers. The expected lifespan of USPs was reported to be approximately 20 years [4].
- *Maintenance and Replacement* The maintenance and replacement of USPs can pose logistical challenges for railway operators. Research endeavours should concentrate on devising cost-efficient and effective maintenance strategies to ensure that USPs continue to deliver the desired benefits over their lifespan.
- *Material Selection* The selection of materials for USPs holds critical importance. Different materials possess varying levels of stiffness and viscoelastic properties, which can influence their performance. Research needs to investigate the optimal material choices for specific track configurations and load conditions.
- *Impact on Track Geometry* The implementation of USPs can affect track geometry and alignment. Researchers should evaluate how USPs impact track stability, alignment, and gauge and develop strategies to mitigate any adverse effects.
- *Environmental Consequences* The environmental repercussions of USPs, including their production, disposal, and potential contributions to noise and vibration, require further examination. The exploration of sustainable materials and manufacturing processes can help minimise their ecological footprint.
- *Optimal Design Parameters* Studies should concentrate on identifying the ideal design parameters for USPs, including stiffness, dimensions, and placement, to achieve the desired reduction in dynamic impacts. These parameters must be adaptable to various track configurations and load conditions.
- *Compatibility with Different Track Types* The performance of USPs may vary based on the type of track, be it ballasted, slab, or transitions between them. Research should address how USPs can be tailored to different track types and setups.
- *Cost–Benefit Analysis* A comprehensive cost–benefit analysis is necessary to evaluate the economic feasibility of implementing USPs. This analysis should encompass initial installation expenses, maintenance costs, and long-term benefits, including reduced maintenance, enhanced passenger comfort, and increased track longevity.

This paper focuses on a process that could be for the considerations listed above, including viscoelastic material evaluation, temperature effects on the dynamic behaviour on the track, more precise track modelling, and optimal parameters selection. Conventional simulation models of USPs have been limited, not accounting for the frequency- and temperature-dependent behaviours of the VE elements. This is where the newly proposed model comes into play. The model focuses on developing a semi-analytical approach that includes the VE properties of USPs and RPs in the transition zones. To achieve this, material testing and parameter estimation steps are performed by a hybrid approach to utilise GMM instead of a fractional derivative model (FDM) in time domain analyses. VE interaction forces between the resilient elements are taken into account with a numerical solution scheme of hereditary integrals [28]. The estimated material parameters are then used in a 3D FEM simulation of the superstructure and semi-analytical solutions. After this, the proposed model is validated with in situ measurements, and receptance functions are utilised to obtain frequency-based characteristics. Finally, the results of the comparisons between KVM and GMM are presented to investigate the effects of ambient temperature on the dynamic response of superstructures. Compared to conventional KVM, the results

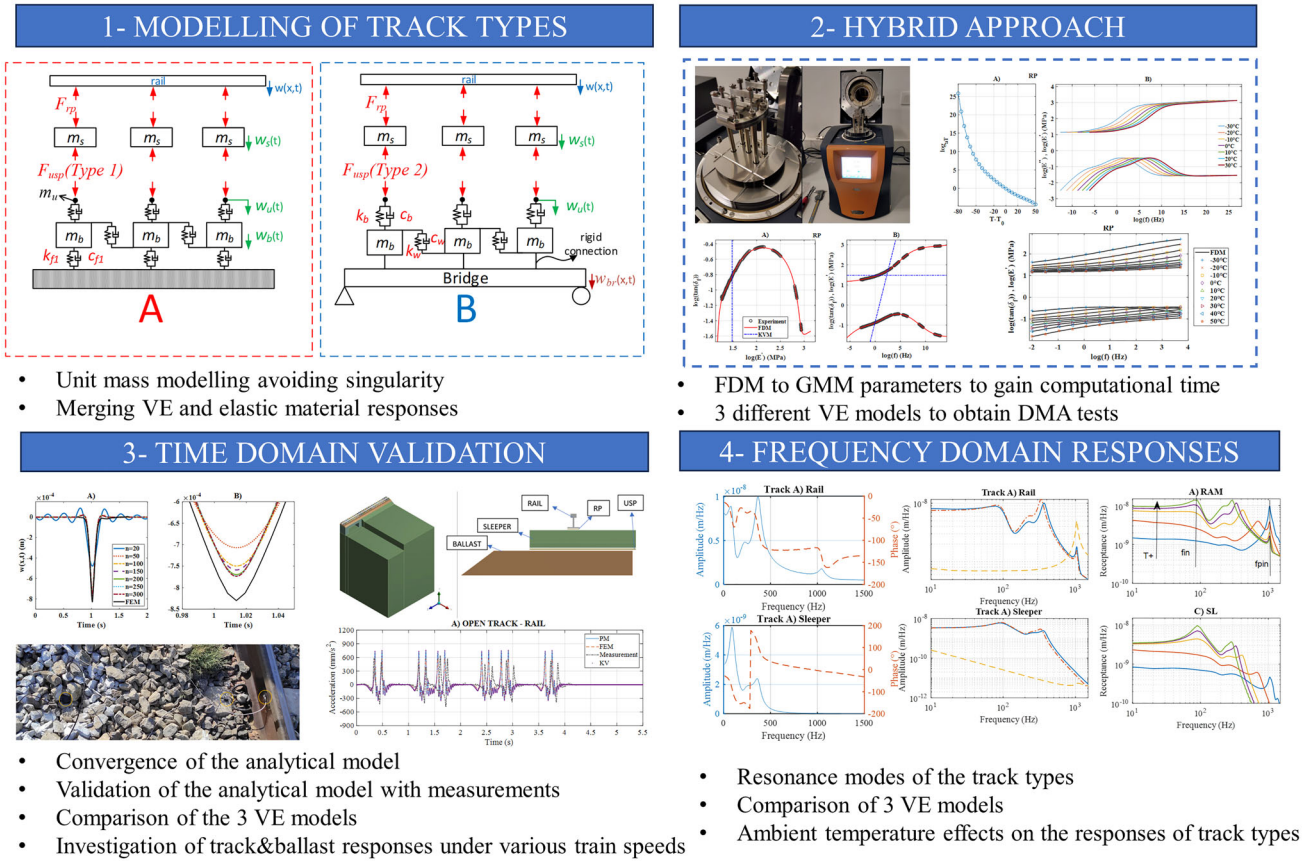


Fig. 1 Flow chart of the study

show better agreement between measurements and GMM. The structure of the study is illustrated in Fig. 1, in addition to the important and useful contributions of each of the steps.

2 Railway Transition Zone Modelling

The transition zone where the soil-bridge-soil foundation is modelled in this study is located in Ankara, as shown in Fig. 2A. The studied line has a straight layout, and there is no curve here. As shown in Fig. 2B, the soil foundations on the east and west sides of the bridge are named as open track. The bridge has 2 symmetric 6-m-long spans. A UIC60 type rail and a HM SKL 14 type fastening system are used in the superstructure. Basalt type rock and B70 pre-stressed concrete type sleepers are the other components. Apart from the methods illustrated in another study [17], the open track (Type A) and the bridge track (Type B) have different USPs. In other words, Type B has a softer USP compared to Type A to decrease the stiffness gradient.

Two types of superstructures are modelled for the transition zone, Track A corresponding to the open track and Track B corresponding to the bridge zone. It is common practice when analysing railway superstructures dynamically to assume sleepers and ballast masses as lumped rigid masses and the rail as a continuous elastic system. Additionally, the RP and USP are considered as elastic spring–dashpot components in classical dynamic analyses. In the proposed model, to account for the stiffness of the USP and ballast, a unit mass is placed between them to avoid mathematical singularity, while the force of the USP acts on it. Although the degrees of freedom increase, the stiffness and damping forces of the ballast and USPs can be calculated separately. This is because the USP model and the ballast spring–dashpot could not be unified due to the VE response calculation of the USP. By adding a unit mass, the integrity of the system is not compromised, and it is kept mathematically stable by avoiding singularity.

An illustration of the superstructure components is shown in Fig. 3. In the superstructure components identified here, elements shown from P_1 to P_{12} are moving loads representing the wheel loads of the train. The mathematical representations of the transition zone are given in the following subsection.

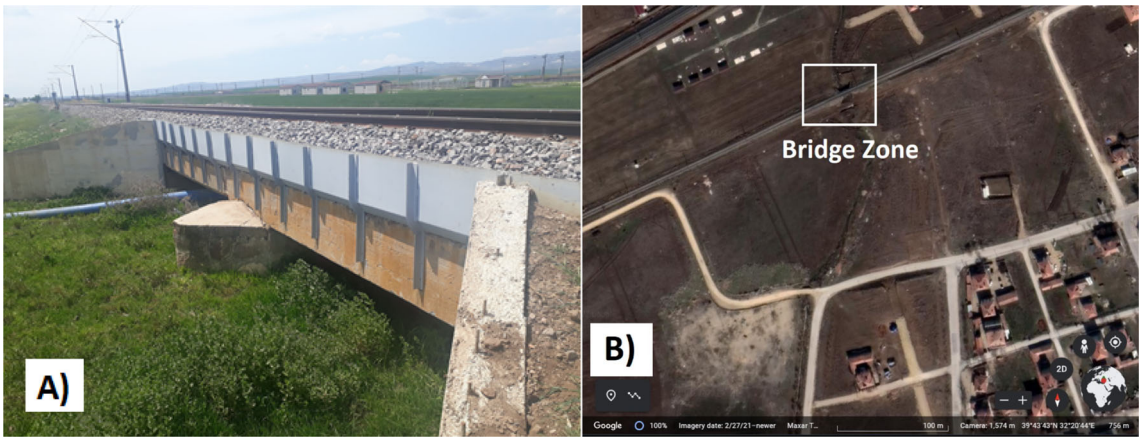


Fig. 2 **A** View of the tested area, **B** Location of the transition zone

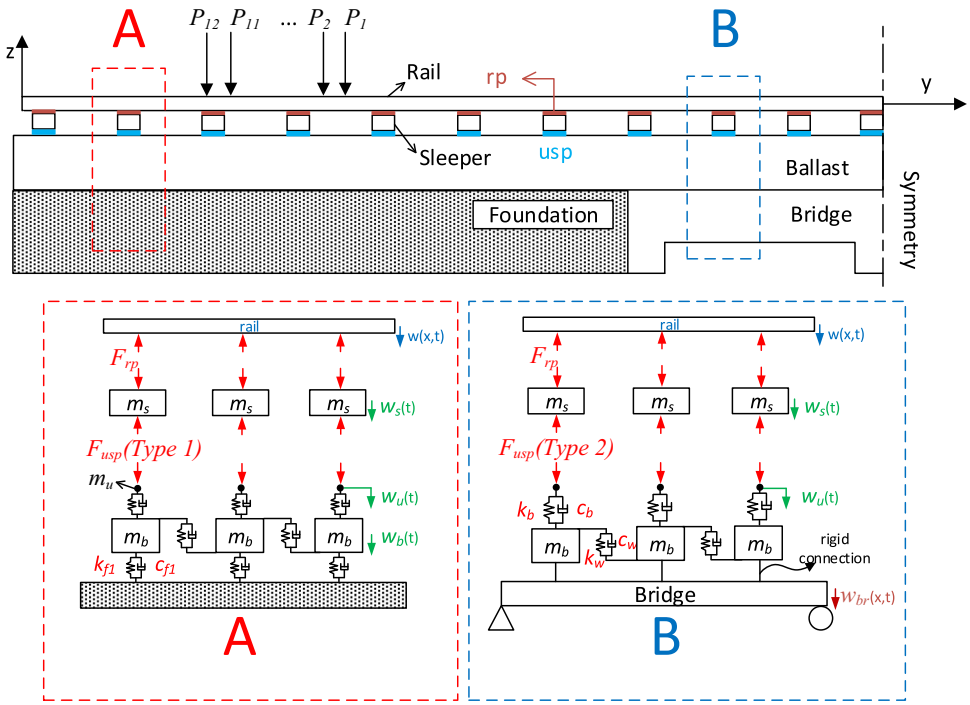


Fig. 3 Components of transition zone superstructure. **A** Track A: open track zone, **B** Track B: bridge zone

2.1 Semi-Analytical Modelling

The partial differential equations represent the vertical translation and rotation of the beam section as w and θ, respectively, even though the rail is represented as a Timoshenko beam (Eqs. 1–2). Differentiations in time and space are represented, respectively, by ($\ddot{}$) and ($''$).

$$\rho A\ddot{w}(x,t)+\kappa AG\left(\theta'(x,t)-w''(x,t)\right)+\sum_{j=1}^{n_p}F_{\text{pad},j}\delta\left(x-L_{p,j}\right)=\sum_{j=1}^{n_v}P_j\delta\left(vt-L_{v,j}\right) \quad (1)$$

$$\rho I\ddot{\theta}(x,t)-EI\theta''(x,t)+\kappa AG\left(\theta(x,t)-w'(x,t)\right)=0 \quad (2)$$

$$w(x,t)=\sum_{i=1}^{n}T_i(t)\phi_i(x),\ \theta(x,t)=\sum_{i=1}^{n}R_i(t)\psi_i(x) \quad (3)$$

$$\phi_i(x)=\sin\left(\frac{i\pi x}{L}\right),\ \psi_i(x)=\cos\left(\frac{i\pi x}{L}\right) \quad (4)$$

where n is the number of sine and cosine modes considered in the approximation. Note that the trigonometric functions in Eq. (4) are selected to satisfy the simply supported boundary conditions. Equations 3–4 are placed into Eqs. 1–2, and the results are then multiplied by the respective mode. After integration via the solution domain, all terms are equated to zero and Eqs. 5–6 are obtained with some algebraic manipulations

[28, 30].

$$\frac{\rho AL}{2}\ddot{T}_i(t)+\frac{\kappa AGL}{2}\left[\left(\frac{i\pi}{L}\right)^2 T_i(t)-\frac{i\pi}{L}R_i(t)\right] + \sum_{j=1}^{n_p} F_{\text{pad},j}\phi_i\left(L_{p,j}\right)=\sum_{j=1}^{n_v} P_j \sin\left(\frac{i\pi\left(vt-L_{v,j}\right)}{L}\right)$$

$$\frac{\rho IL}{2}\ddot{R}_i(t)+\frac{EIL}{2}\left(\frac{i\pi}{L}\right)^2 R_i(t) \tag{5}$$

$$+\frac{\kappa AGL}{2}\left[R_i(t)-\frac{i\pi}{L}T_i(t)\right]=0 \tag{6}$$

The sleepers, unit masses, and ballast are modelled as lumped masses, symbolised as m_s, m_u, and m_b, respectively. Additionally, n_p is the number of RPs in Eqs. 5–6,k_b, k_f,c_b, and c_f are the ballast stiffness, support stiffness, ballast damping coefficient, and support damping coefficients, k_w and c_w are the stiffness and damping coefficients of interactions of ballast masses, w_s, w_u, and w_b are the jth vertical displacements of the sleeper, unit mass, and ballast mass, respectively. The coefficients $k_{f,j}$ and$c_{f,j}$ should be adjusted according to Track B, because the vertical stiffness of the support varies before and over the bridge. Thanks to m_u in Eq. 8, the elastic response of the ballast and the VE response of the USP can be implemented by preventing the singularity of the system.

$$m_s\ddot{w}_{s,j}(t)-F_{\text{pad},j}+F_{\text{usp},j}=0 \quad j=1,2,\ldots,n_p \tag{7}$$

$$m_u\ddot{w}_{u,j}(t)+k_b\left(w_{u,j}(t)-w_{b,j}(t)\right) + c_b\left(\dot{w}_{u,j}(t)-\dot{w}_{b,j}(t)\right)-F_{\text{usp},j}=0 \tag{8}$$

$$m_b\ddot{w}_{b,j}(t)+\left(k_b+k_{f,j}+2k_w\right)w_{b,j}(t) + \left(c_b+c_{f,j}+2c_w\right)\dot{w}_{b,j}(t)-Fbw_j(t)=0 \quad j=1,2,\ldots,n_p \tag{9}$$

$$Fbw_j(t)=k_b w_{u,j}(t)+k_w w_{u,j+1}(t)+k_w w_{u,j-1}(t) + c_b\dot{w}_{u,j}(t)+c_w\dot{w}_{u,j+1}(t)+c_w\dot{w}_{u,j-1}(t) \tag{10}$$

The bridge in Track B is modelled as an Euler–Bernoulli beam due to its low-frequency characteristic, contrary to the Timoshenko theory that is utilised for high-frequency behaviour. By using trigonometric series in Eq. 11, the governing ODEs of the bridge are calculated as in Eq. 12. In Eq. 13, $F_{f,l}$ is the interaction force between the ballast and the bridge, m_{br}, L_{br}, E_{br}, and I_{br} are the parameters of the mass of the bridge, length of the bridge, Young's modulus of the bridge, and inertia of the bridge, and n_{p2} and n_{br} are the number of sleepers on the bridge and the number of the trigonometric terms of the bridge, respectively. The other interaction forces in Eq. 1 are updated as in Eq. 14 according to the relative displacement and relative velocity between the bridge masses.

$$w_{br}(x,t)=\sum_{k=1}^{n_{br}} T_{br,k}(t)\phi_{br,k}(x),\ \phi_{br,k}(x)=\sin\left(\frac{k\pi x}{L}\right) \tag{11}$$

$$\left(\frac{m_{br}L_{br}}{2}+\sum_{l=1}^{n_{p2}} m_b w_{br}\left(L_{pbr,l},t\right)\right)\ddot{T}_{br,k}(t)+\frac{L_{br}E_{br}I_{br}}{2}\left(\frac{k\pi}{L_{br}}\right)^4 T_{br,k}(t) = \sum_{l=1}^{n_{p2}} F_{f,l}w_{br}\left(L_{pbr,l},t\right)$$

$$k=1,\ldots,n_{br} \tag{12}$$

$$F_{f,l}=k_{b,j}\left(w_{u,j}(t)-w_{br}\left(L_{pbr,l},t\right)\right)+c_{b,j}\left(\dot{w}_{u,j}(t)-\dot{w}_{br}\left(L_{pbr,l},t\right)\right)$$

$$l=1,\ldots,n_{p2} \quad j=n_{p1}+1,\ldots,n_p \tag{13}$$

$$Fbw_j(t)=k_b w_{br}\left(L_{pbr,l},t\right)+c_b\dot{w}_{br}\left(L_{pbr,l},t\right)+k_w w_{br}\left(L_{pbr,l+1},t\right) + c_w\dot{w}_{br}\left(L_{pbr,l+1},t\right)+k_w w_{br}\left(L_{pbr,l-1},t\right) + c_w\dot{w}_{br}\left(L_{pbr,l-1},t\right)$$

$$l=1,\ldots,n_{p2} \quad j=np+1,\ldots,np2 \tag{14}$$

One can represent equations of motion in matrix form as follows,

$$\mathbf{M_G}\ddot{\mathbf{q}}+\mathbf{K_G}\mathbf{q}+\mathbf{C_G}\dot{\mathbf{q}}=\mathbf{F_G} \tag{15}$$

$$\begin{bmatrix}\mathbf{M_R}&0&0&0&0\\0&\mathbf{M_S}&0&0&0\\0&0&\mathbf{M_U}&0&0\\0&0&0&\mathbf{M_B}&0\\0&0&0&0&\mathbf{M_{BR}}\end{bmatrix}\begin{Bmatrix}\ddot{q}_R\\\ddot{W}_S\\\ddot{W}_U\\\ddot{W}_B\\\ddot{q}_{BR}\end{Bmatrix} + \begin{bmatrix}\mathbf{K_R}&0&0&0&0\\0&0&0&0&0\\0&0&\mathbf{K_B}&-\mathbf{K_B}&0\\0&0&-\mathbf{K_B}&\mathbf{K_{BFW}}&-\mathbf{K}_{\mathbf{FBR}}^T\\0&0&0&-\mathbf{K_{FBR}}&\mathbf{K_{BR}}+\mathbf{K_{BRF}}\end{bmatrix}\begin{Bmatrix}q_R\\W_S\\W_U\\W_B\\q_{BR}\end{Bmatrix} + \begin{bmatrix}0&0&0&0&0\\0&0&0&0&0\\0&0&\mathbf{C_B}&-\mathbf{C_B}&0\\0&0&\mathbf{C_{BW}}&\mathbf{C_{BFW}}&-\mathbf{C}_{\mathbf{FBR}}^T\\0&0&0&-\mathbf{C_{FBR}}&\mathbf{C_{BRF}}\end{bmatrix}\begin{Bmatrix}\dot{q}_R\\\dot{W}_S\\\dot{W}_U\\\dot{W}_B\\\dot{q}_{BR}\end{Bmatrix} = \begin{Bmatrix}\{P_V\}+\{F_{\text{PAD},R}\}\\\{F_{R,\text{PAD}}\}-\{F_{\text{USP}}\}\\\{F_{\text{USP}}\}\\0\\0\end{Bmatrix} \tag{16}$$

Global mass, global stiffness, global damping matrices, and global force vectors are symbolised as $\boldsymbol{M}_G$, $\boldsymbol{K}_G$, $\boldsymbol{C}_G$, and $\boldsymbol{F}_G$. q, $\dot{q}$, and $\ddot{q}$ are, respectively, the merged vectors of

Table 1 Dynamic model parameters of the transition zone

Parameters	Definition	Value	Unit	Parameters	Definition	Value	Unit
ρ	Rail density	7850	Kg m^3	v	Train speed	65	Km/h
A	Rail cross-sectional area	7636×10^{-6}	m^2	$P_{1,\ldots,12}$	Moving loads	50	kN
L	Total length of track	17.4	m	k_{b}	Ballast stiffness	43.6×10^6	N/m
κ	Shear correction factor	0.34	–	c_{b}	Ballast damping	12×10^3	N s/m
υ	Poisson's ratio of rail	0.3	–	k_w	Ballast shear stiffness	39.2×10^6	N/m
E	Young's modulus of rail	200	GPa	c_w	Ballast shear damping	40×10^3	N s/m
G	Shear modulus of rail	76.9	GPa	$k_{f,1,\ldots,np1}$	Support stiffness of Type A	57×10^6	N/m
I	Inertia of rail cross section	3053×10^{-8}	N/m^4	$c_{f,1,\ldots,np1}$	Support damping of Type A	9.9×10^3	N s/m
n	Number of terms of open track	250	–	n_p	Total number of sleepers	77	–
n_{br}	Number of terms of bridge	20	–	n_{p1}	Number of sleepers in Type A	69	–
L_p	Sleeper distance	0.6	m	n_{p2}	Number of sleepers in Type B	8	–
Δt	Time step	10^{-5}	s	a_{pad}	Rail pad width	161	mm
m_{s}	Sleeper mass	168.5	kg	d_{pad}	Rail pad length	150	mm
m_{b}	Ballast mass	258.79	kg	h_{rp}	Rail pad thickness	6	mm
m_{u}	Unit mass	1	kg	a_{usp}	USP width	300	mm
m_{br}	Bridge mass per length	3795	kg/m	d_{usp}	USP length	1300	mm
L_{br}	Bridge length	3.6	m	h_{usp}	USP thickness	10	mm
E_{br}	Bridge Young's modulus	30	GPa	I_{br}	Inertia of bridge cross section	0.0703	N/m^4

displacement, velocity, and acceleration as well as containing unknown time coefficients of the rail, sleeper, ballast, unit mass, and the bridge. The submatrices of Eq. 15 are shown in Eq. 16, where open forms are presented in Appendix B. The parameters of the transition zone's dynamic model are given in Table 1. The generalised matrices of the railway superstructure are solved by using MATLAB 2021 with the built-in function ODE8 [28]. The results of the VE force calculations (F_{pad} and F_{usp}) are given in the next section.

2.2 Hybrid Approach for Viscoelastic Material Model

In this section, classical linear VE material models and a fractional order derivative VE material model with ten parameters [27] are introduced, and then, an existing hybrid approach [28] is applied to the dynamic mechanical analysis (DMA) test results of the RP and USPs. After the construction of the master curve for one temperature by using the Wicket plot, the master curve is shifted for six selected temperatures in the frequency domain. This provides a more accurate path from the experimental points to the VE models. In addition to the model developed in a previous study [31], this paper differs from other studies in terms of the solution developed to avoid singularities, the application of the method to a transition region, the verification of the method by comparing the results of the experimental study to a real system, and the integration of the DMA results into the model. By using the hybrid approach, we find GMM coefficients instead of FDM parameters; hence, calculation effort can be decreased drastically.

Classical integer derivative material models fail to predict frequency-dependent properties across a wide frequency spectrum. On the other hand, fractional derivative order models are highly capable in representing VE properties in all frequency ranges. Springs and spring-pots make up FDMs, while springs and dashpots make up integer derivative models (classical VE models). The spring-pots (Fig. 4A) that are represented by X and β, on the other hand, not only exhibit elastic/VE behaviours but also have stress–strain relationships, and they are shown via fractional time derivative terms. The elastic properties of classical VE models are represented by the springs, whereas damping properties are represented by dashpots (Fig. 4B, C). In this paper, GMM is utilised in the dynamic analyses to reflect RP and USP material properties.

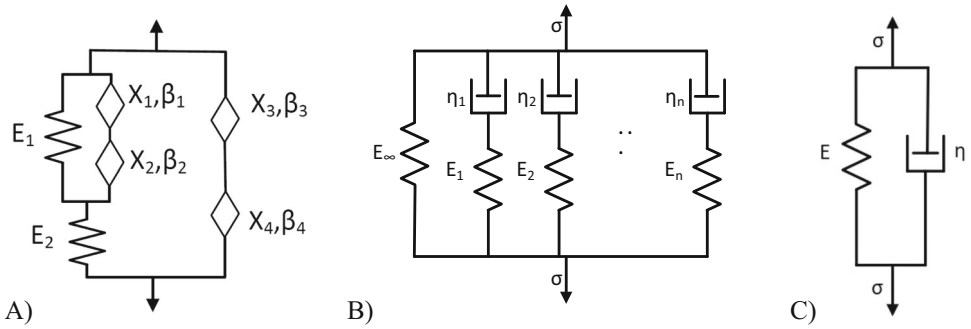


Fig. 4 **A** Ten-parameter FDM [27], **B** GMM or Prony series **C** KVM

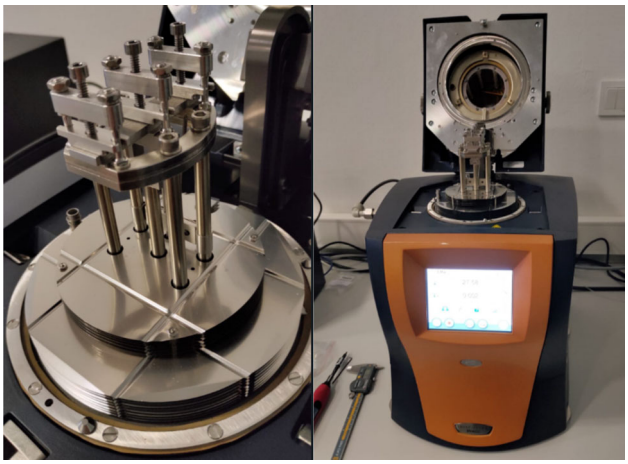


Fig. 5 TA Instruments TGA 5500 with dual cantilever bending apparatus

A hybrid approach is proposed to exploit the advantages of FDM and GMM presentations and minimise their drawbacks [28]. The master curve in the frequency domain is created through the application of a ten-parameter FDM. The parameters of this model are identified using genetic algorithms with Wicket plot data. This master curve, along with shift factors, is employed to generate DMA at specific temperatures and frequency ranges. Subsequently, data for the loss factor and storage modulus are extracted from the master curve. The GMM parameters are then determined for time domain analyses at a chosen temperature and within a specified frequency range (0.1 Hz $< f <$ 5000 Hz).

DMA experiments are conducted by utilising a TA Instruments TGA 5500 device, as illustrated in Fig. 5. The pad samples, measuring 50 × 13 × 3 mm, undergo a dual cantilever bending test procedure. To maintain temperature uniformity within the samples, a controlled heating rate of 3 °C/min is employed during the tests. The tests are conducted three times in the temperature range of − 80 °C to + 50 °C (10 °C intervals).

Figure 6 displays the experimental points and calculated FDM curves for three distinct pads. The figures depict Wicket plots, illustrating the relationship between the storage modulus and the loss factor on the left side. The corresponding master curves, obtained at the reference temperature (0 °C), are presented on the right side of the figures. The top section displays storage modulus curves, while the bottom section shows loss factor curves. Base 10 logarithmic numbers are used to visualise the plots. The storage modulus and loss factor are E' and $\tan\delta_f$, respectively. The ten-parameter FDM demonstrates excellent consistency with the experimental data across a broad frequency spectrum. However, KVM is not appropriate for the experimental data due to the constant value of the storage modulus and the linearly varying frequency-dependent loss factor. In case of a constant loss factor of KVM, the whole range cannot be reflected, except for its own frequency and its observation as one point.

As shown in Fig. 7, the FDM curves at different temperatures are shifted, and the shift factors change with temperature for each pad. The data at elevated temperatures are positioned on the right side of the figure. Table 4 provides the identified shift factors and FDM parameters for the respective pads.

FDM is an effective method to represent VE behaviours, but it poses challenges in terms of software and processing costs for dynamic analyses. GMM is an alternative way that employs two to seven arms (branches) to approximate FDM data into a specific frequency range. The parameters of GMM are calibrated to match the storage modulus and loss factor data of the VE material at various temperatures between 0.01 and 5000 Hz by using a hybrid approach [28]. The GMM coefficients of the elastomeric pads are presented in Tables 5, 6, and 7 and illustrated in Fig. 8.

2.3 Finite Element Modelling

The finite element modelling (FEM) of transition zone is presented in this subsection. To compare the solution efficiency and accuracy of the proposed model, an FE model is generated. The I shape is used to simplify the UIC60 rail for better meshing. Furthermore, a 50-m-deep soil foundation is put under the ballast to prevent wave reflection. Figure 9 shows the FEM of the superstructure. Two different zones

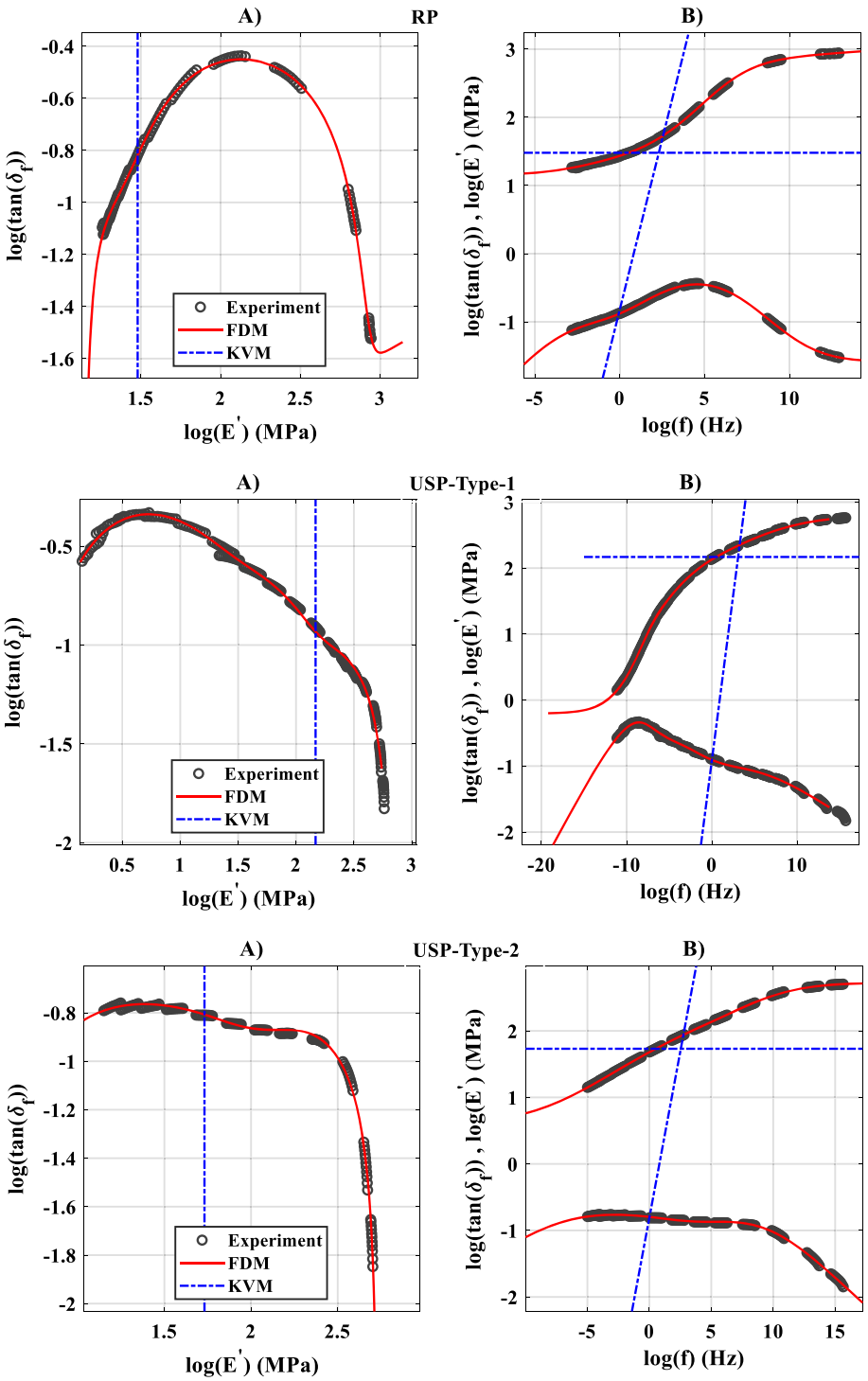


Fig. 6 FDM, KVM, and experimental data comparison **A** Wicket plot, **B** Storage modulus and loss factor for wide frequency range

are given in Fig. 9A. The symmetry condition is applied to the model according to the *X* axis (Fig. 9B). A magnified side view of the meshed parts is given in Fig. 9C. To prevent uncertain vibrations, measurements and modelling are carried out for a well-conditioned track. In other words, wheels and rail surfaces are grinded, and the track is re-tamped and without voids. The geometry of the FE model of the track superstructure is presented in Fig. 9.

The FEM uses the elastic material details as given in Table 2. The VE parameters obtained for RP and USP are utilised with a seven-arm GMM for the material section of ANSYS to represent VE behaviours (Table 3). To define

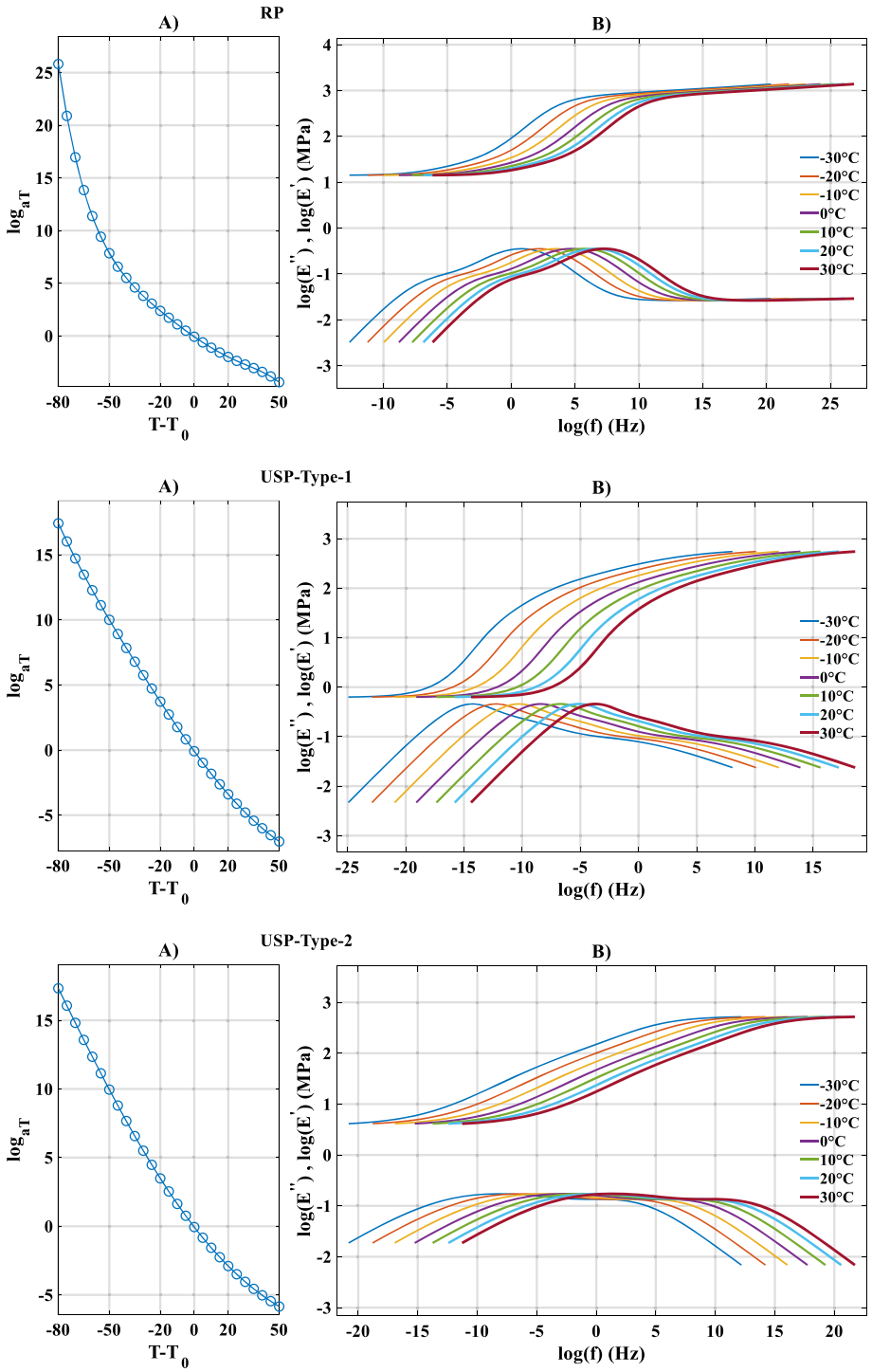


Fig. 7 **A** Shift factors, **B** Shifted master curves for selected temperatures

them, spring parameters (E′s) must be normalised according to Eq. 17. These normalised values are represented by E_{ni}, while the summation of all E′s is shown by E_0.

$$M(t) = E_0\left[\frac{E_\infty}{E_0} + \sum_{i=1}^{N} E_{ni}\exp(-t/\tau_i)\right] \tag{17}$$

A moving load cannot be defined directly in ANSYS. Hence, a distributed load analogous to the Dirac delta function is employed [28, 30]. The FEM solution takes 100 h on a workstation (AMD Threadripper 3970x @3.7 GHz & 128 GB of RAM).

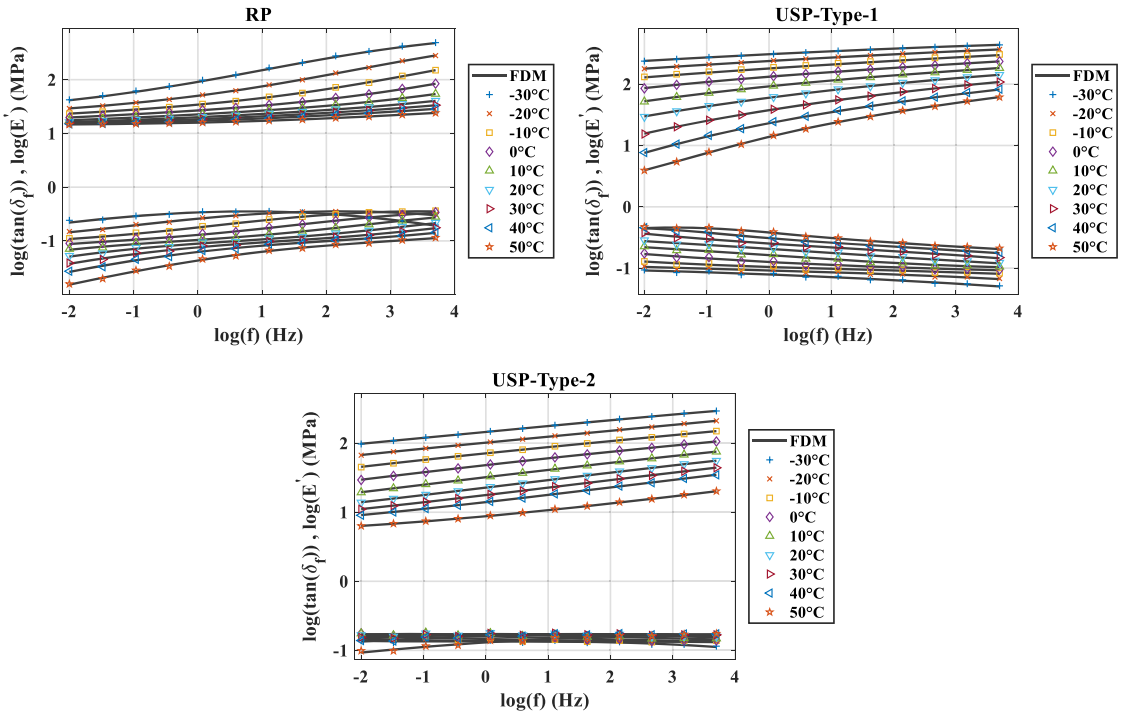


Fig. 8 Identified GMM curves at desired temperatures for narrow range

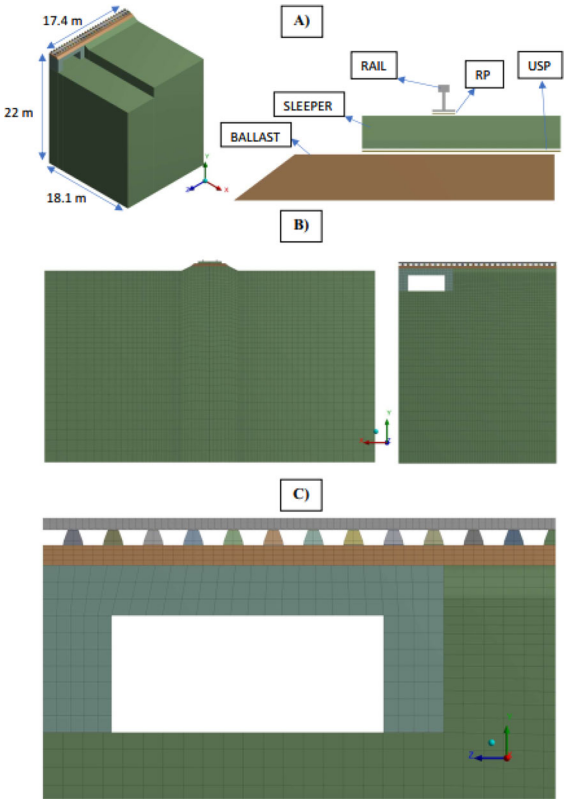


Fig. 9 **A** Geometry, **B** Meshing with symmetry boundary condition, **C** Meshing magnified side view

3 Time Domain Analyses and Validation

3.1 Convergence

While convergence studies are carried out in this subsection, the number of terms is decided in terms of elapsed time and the midpoint deflection of the rail. In the convergence studies, one moving load is applied to the structure. Then, the damping capacities of the USPs are compared. With the decided number of terms, calibration studies are performed, and thus, the numerical and semi-analytical transition models are validated via field tests. Other studies are also performed to analyse the effects of the parameters on the dynamic responses of the superstructures.

The partial differential equations of the transition zone are transformed into ordinary differential equations (ODEs) with Galerkin's method. Here, the number of terms is important for estimating the dynamic responses of the model. Hence, convergence studies are carried out for one moving load as shown in Fig. 10A. This moving load is acting on the superstructure from the beginning to the end with a constant velocity of 65 km/h. The midpoint deflection results of the rail are illustrated for solutions with different numbers of terms. On the right side of the figure, a magnified area of the midpoint deflection is given. It is seen that 250 or 300 terms are applicable for the later simulations. However, solution times must be assessed.

Table 2 Properties of the elastic constants of the components in the ANSYS program

Part	Young's modulus (GPa)	Density (kg/m^3)	Poisson's ratio	Mesh size (mm)
Rail	200	7850	0.3	20
Sleeper	30	2530	0.2	100
Ballast	0.13	1500	0.2	150
Soil Foundation	0.2	2000	0.3	300–700
Rail pad (E_0)	55.475×10^{-3}	1000	0.4	50
USP Type 1 (E_0)	167.614×10^{-3}	1077	0.4	100
USP Type 2 (E_0)	69.164×10^{-3}	1077	0.4	100

Table 3 Material section VE constants of the pads at 20 °C in ANSYS

Pads	Parameters	Unit	Arm 1	Arm 2	Arm 3	Arm 4	Arm 5	Arm 6	Arm 7
RP	E_{ni}	–	0.3295	0.1347	0.0896	0.0622	0.0464	0.0326	0.0235
	τ_i	s	0.0001	0.001	0.01	0.1	1	10	100
USP Type 1	E_{ni}	–	0.1857	0.1384	0.1374	0.1251	0.1098	0.0893	0.0798
	τ_i	s	0.0001	0.001	0.01	0.1	1	10	100
USP Type 2	E_{ni}	–	0.2372	0.1548	0.1334	0.1046	0.0826	0.0618	0.0525
	τ_i	s	0.0001	0.001	0.01	0.1	1	10	100

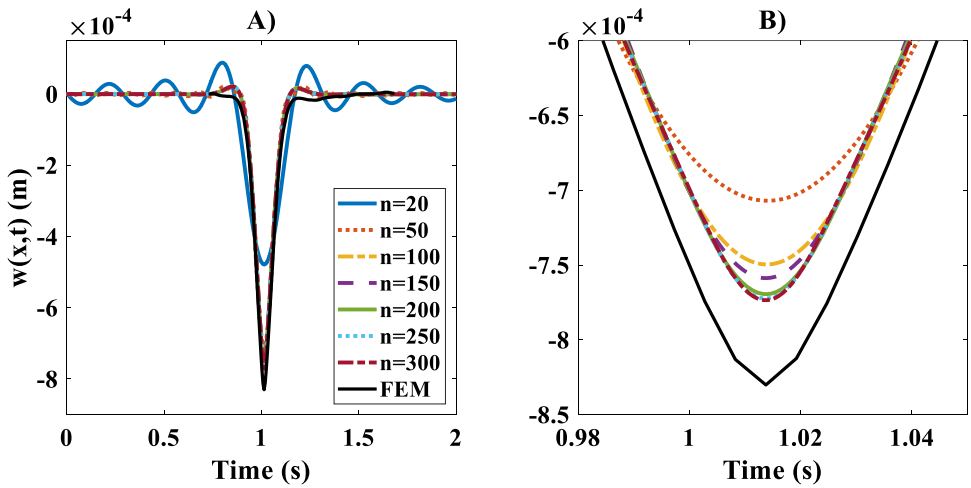


Fig. 10 Midpoint deflection time history of the rail in open track for one load at 20 °C **A** Total time, **B** Magnified area

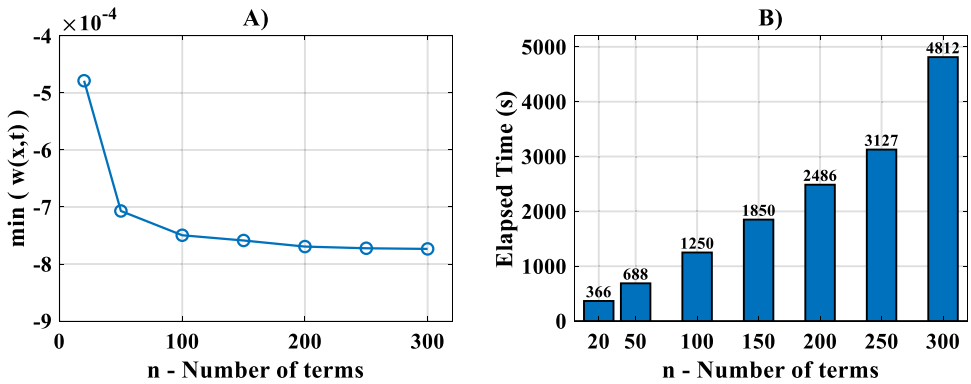


Fig. 11 Convergence study **A** Minimum deflections, **B** Elapsed times

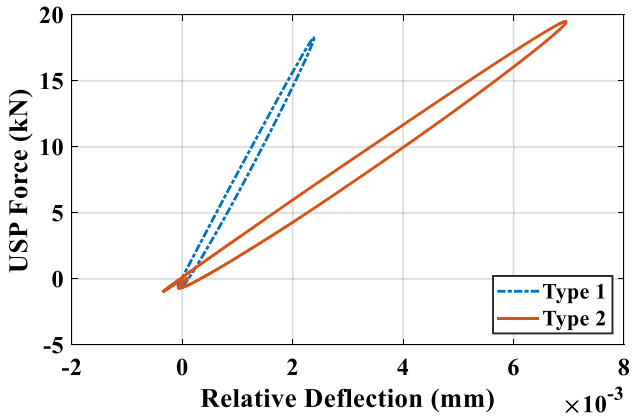


Fig. 12 Force–displacement curves at midpoint USPs of the open track and bridge at 20 °C

The next convergence study is about calculation times for solving ODEs. The midpoint deflections of the rail are visualised in Fig. 10, and now, the elapsed times are compared. In Fig. 11, the maximum magnitude of the deflections is shown on the left side. On the right side of Fig. 11, computation times are given with the respect to the number of terms. One can observe that the 250- and 300-term results are slightly different. However, the elapsed time of 300 terms is 1.5 times of the 250-term solution. As a result, the use of 250 terms is decided for the remaining analyses.

The hysteresis curves of the USP Types 1 and 2 are illustrated in Fig. 12 to understand their damping capacities. One can see that 2.73 times more energy is dissipated by the Type 2 model than Type 1 as the comparison of areas enclosed by the curves indicate.

3.2 Validation with Measurements

To verify the proposed mathematical models, a field measurement is carried out for an unloaded 6-bogie 12-wheel commuter train with axle spacings as shown in Fig. 13 B at a speed of 65 km/h. KVM and GMM representations are used to compare the VE modelling results of the elastic elements. All simulations are performed with material parameters at 20 °C, as the weather was dry and windless, and the temperature was 20 °C. As shown in Fig. 3, two types of superstructures are already introduced as Track A and Track B with 0.6 m of spacing, and they have USP Types 1 and 2, respectively. ICP type accelerometers are mounted on the rail web and sleeper, while MEMS type accelerometers are mounted on the ballast. The ICP 50 g sensor on the rail, the ICP 10 g sensor on the sleeper, and the MEMS 50 g sensor on the ballast are recorded at a sampling rate of 2000 Hz as shown in Fig. 13A.

According to fastening distance excitations [19, 31], a 30 Hz low-pass filter is applied to the stored accelerations to minimise the negative effects induced by random excitations of the rail and wheel surfaces. The value of the filter frequency is calculated via the ratio of train speed (65 km/h = 18 m/s) and sleeper distance (0.6 m) as filter frequency = (18 m/s)/(0.6 m) = 30 (Hz). The measured accelerations of 12 wheels are shown clearly in Figs. 14, 15, and 16. A certain lag between models and test results is observed from the first axle to last one due to the decreasing speed of the manually controlled train. The measured data are indicated by black dot-dashed lines, the dotted curves represent the KVM-integrated superstructure with constant damping, and the red dashed line and blue continuous lines correspond to the FEM and proposed method (PM) results, respectively. Additionally, the results of two types of railway tracks are compared to each other.

The maximum measured accelerations at the rail are around 600 mm/s^2. Sleeper accelerations are stored between 300 and 600 mm/s^2. Ballast accelerations are measured in a range of 15–140 mm/s^2. The maximum values of the sleeper and ballast accelerations decrease in Track B as illustrated in Figs. 15 and 16 due to the USP Type 2. For all accelerations, especially the ones on the sleeper and ballast, the proposed model depending on the combination of FDM and GMM shows better agreement with FEM and measurement compared to the KV model.

On the other hand, voided (hanging) sleeper problems can exist in the approaching zones, where contact between the sleeper and the ballast is lost [32–34]. Therefore, ballast particles near the void are exposed to high stress, and finally, track deterioration is experienced. Nevertheless, the voided sleeper issue is not considered in our mathematical model, and therefore, the test zone is re-tamped and fixed against possible corruptions before the measurements.

The maximum forces of the USPs are compared under various train speeds. To assess the force reaction of the USPs, variations of the maximum forces of USPs are given in Fig. 17. An abrupt change is observed at the bridge entrance because of the abrupt stiffness change at the boundaries as seen in a previous paper [32]. Thus, there is a chance for improvement with proper USP integration or structural improvements at the boundaries of the bridge. Furthermore, the maximum ballast accelerations are shown in Fig. 18. The vibration levels of the ballast observed at 160 km/h are almost five times larger than those under the tested train speed. For the investigation of ballast degradation and deformation, ballast vibrations are crucial.

3.3 Frequency Domain Analyses

After the time domain responses are discussed, to analyse the frequency responses of the superstructure, receptance simulations are carried out. The receptance functions and phase

diagrams of the superstructures are shown in Fig. 19. The system is excited at the midspan of the rail, and the responses are taken from the rail (midspan) and the sleeper. There are mainly three types of resonance modes in the ballasted superstructures [18, 33, 34]:

1. The entire track vibrates in phase (f_{in}): the rail, sleeper, and ballast move in the same direction between 40 and 140 Hz. The global stiffness of the superstructure dominates this mode (Track A: 40 Hz, Track B: 60 Hz).
2. The rail and sleeper vibrate out of phase (f_{out}): the rail and sleeper move independently and can be seen between 200 and 600 Hz. The stiffness of the rail pads dominates this mode (Track A: 360 Hz, Track B: 360 Hz).
3. Pinned–pinned mode (f_{pin}): if the rail is excited at the midspan, the midpoint of the rail moves, but the support point of the rail stays still. The span length of the rail dominates this mode and is seen at around 1000 Hz. Here, this mode is seen in both superstructures at around 1044 Hz.

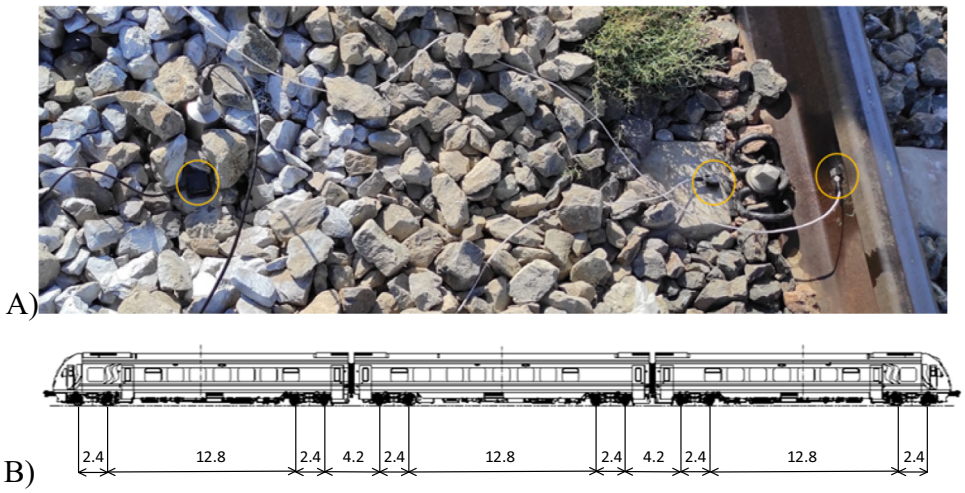


Fig. 13 **A** Sensors at the test field, **B** Commuter train axle distances in metres

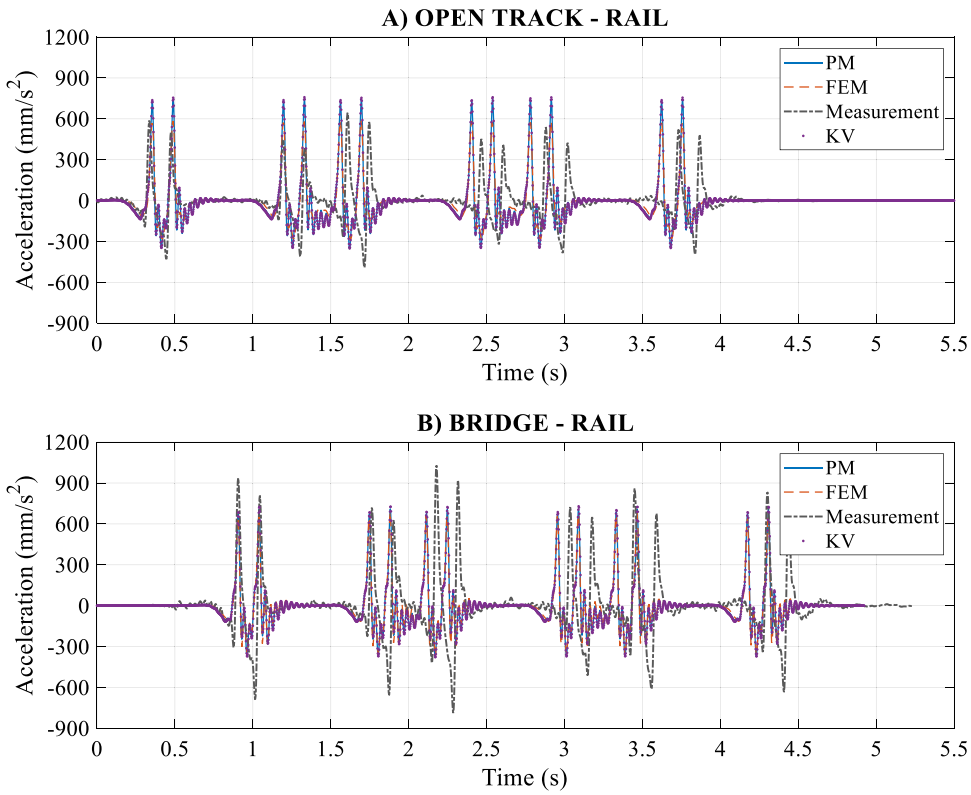


Fig. 14 Rail accelerations

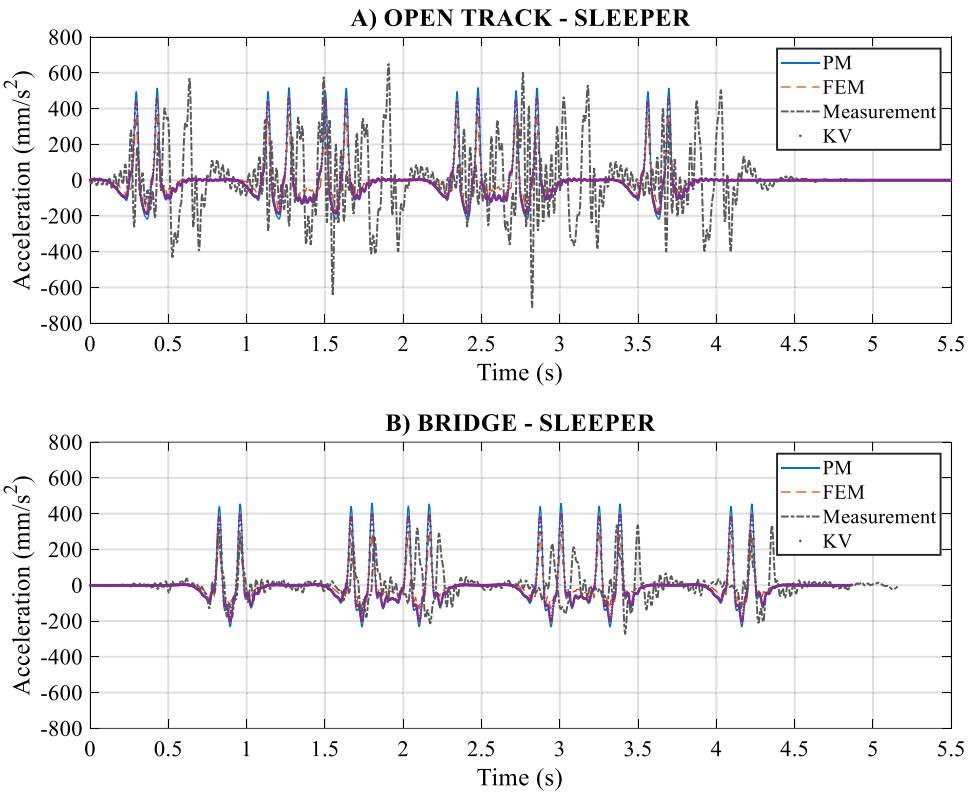


Fig. 15 Sleeper accelerations

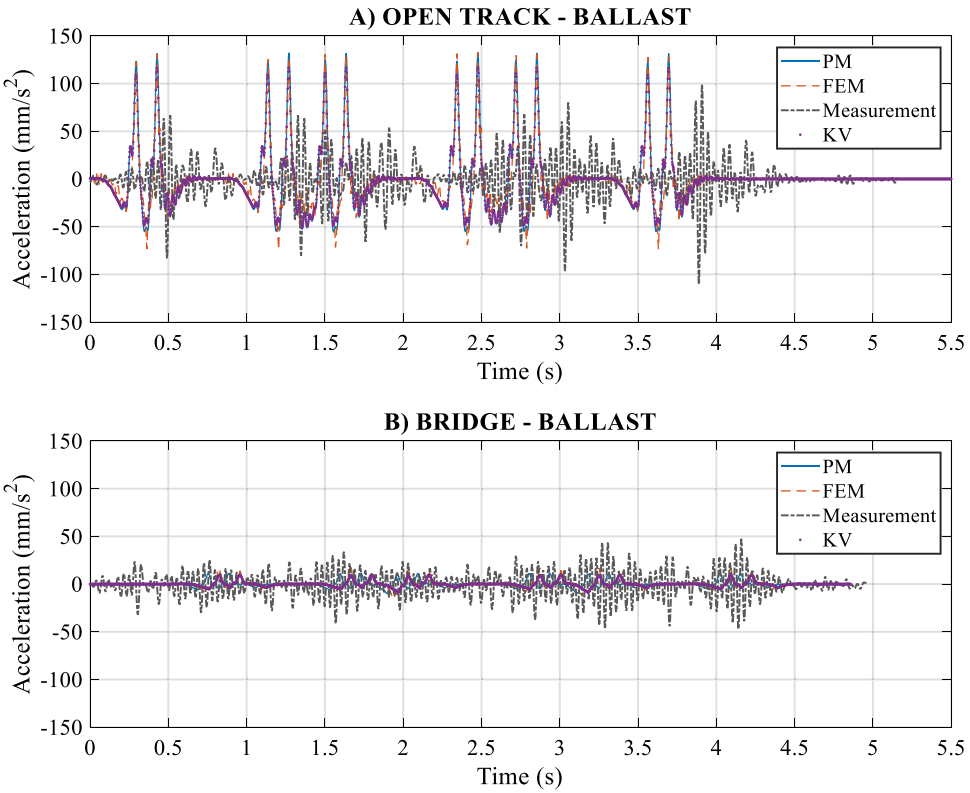


Fig. 16 Ballast accelerations

In both structures, while the sleeper appears to experience a resonant frequency, the rail exhibits anti-resonance (f_s). The global stiffness of the superstructure is important (Track A: 150 Hz, Track B: 66 Hz). In addition to this, there can be certain extra resonance modes, particularly on the Track B rail. The second vertical resonance mode (f_{v2}) looks like a full superstructure mode, while long bending waves accompany it at 150 Hz.

After specifying the characteristic behaviours of the structures, one can vary materials to make improvements on the dynamic behaviours. KVM has two options about frequency dependency of the constant (KVc) or variable (KVv) loss factor as shown in Fig. 6. The constant loss factor has a single value that applies to the entire frequency range at one

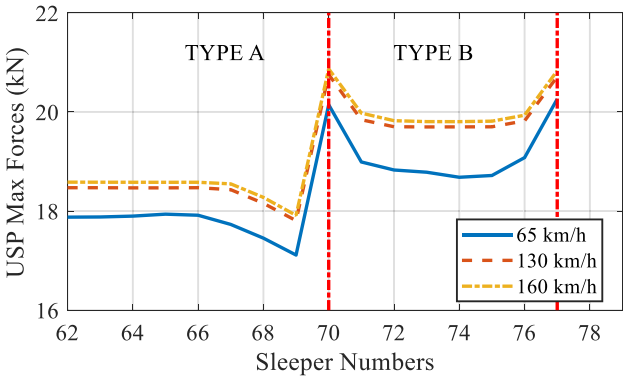


Fig. 17 Maximum USP forces at different train speeds

Fig. 18 Maximum ballast accelerations at different train speeds

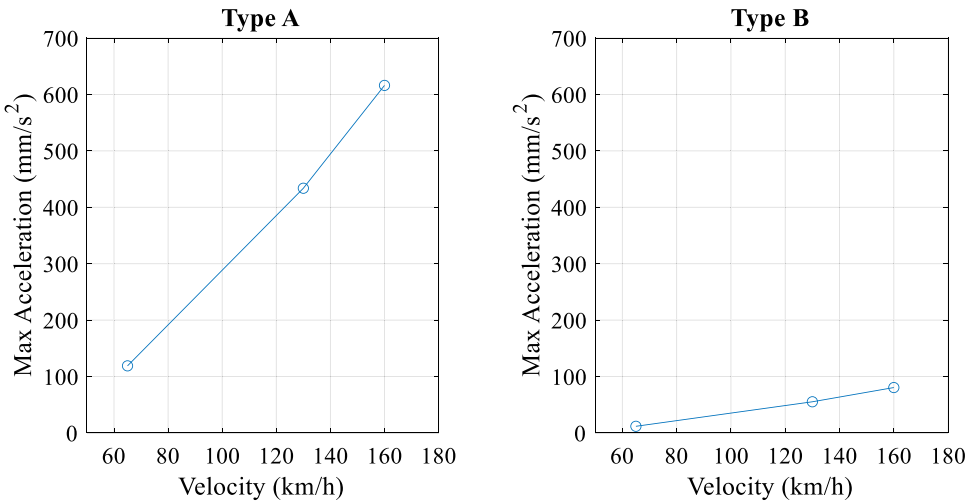
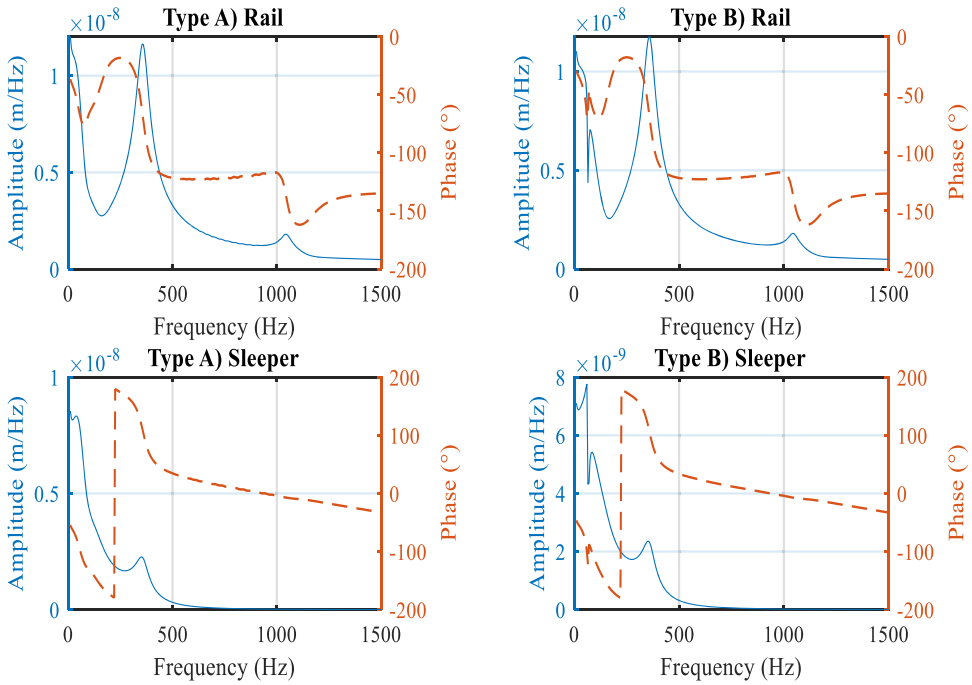


Fig. 19 Amplitudes and phase angles of the resonance modes



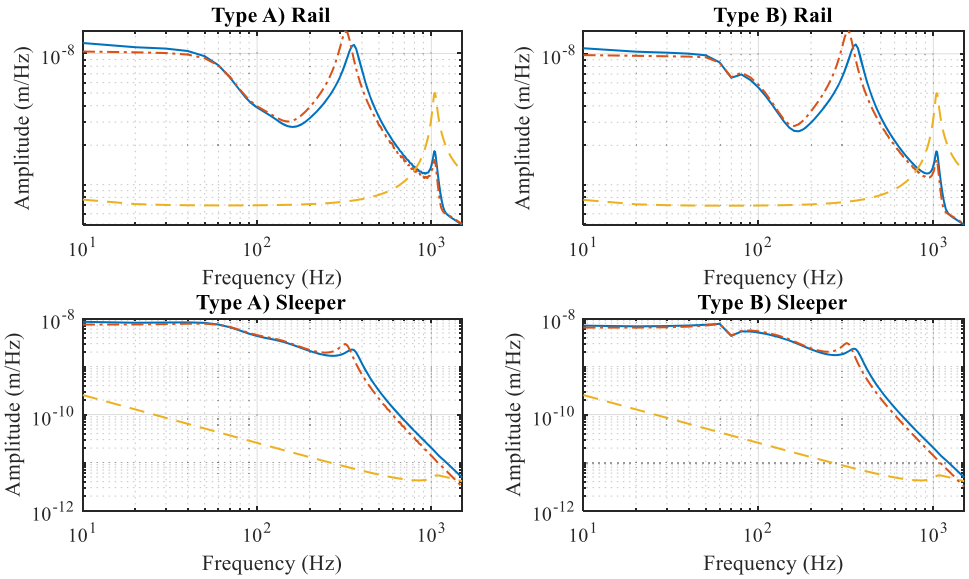


Fig. 20 Effects of the material models on the receptance functions (-:GMM, -.: KVc, --: KVv)

temperature. As shown in Fig. 20, while KVv produces unrealistic results, KVc fails to account for the f_{out} resonance mode. Except stiffness-related modes (f_{in}, f_{out}), f_{pp} is not affected by the variation in stiffness. This is because pad stiffness has far less contribution to this mode. Resonance peaks are clearly separated above 100 Hz, while KVc shows a 5% smaller amplitude below 50 Hz.

To investigate the effects of temperature on the dynamic behaviours of the superstructures, five different temperatures (− 30 °C, − 10 °C, 10 °C, 30 °C, and 50 °C) are selected and applied to the receptance functions as demonstrated in Figs. 21 and 22. RAM, ROS, SL, and BL represent the rail at the midpoint, rail on the support, sleeper, and ballast, respectively. $T+$ indicates the temperature increment. At ROS, the rail is excited and measured from the support (fastening) point.

The USPs are produced from viscoelastic materials, and they have mechanical properties sensitive to temperature changes. Therefore, Figs. 21 and 22 show that the out-of-phase frequency, f_{out}, shifts considerably with temperature changes. On the other hand, the f_{pin} frequency is not sensitive to the stiffness of the elastomer elements and remains almost constant at varying temperatures. As the temperature decreases, f_{out} shifts so much to right-hand side of the figure that it merges with f_{pin} so that the out-of-phase frequency, which is related to the relative motion of the rail and the sleeper, disappears. This is due to the increase in the stiffness of RPs and USPs with the decreasing temperature.

In another study [10], the authors considered USPs with different stiffness to see the dynamic response of the superstructure. It is seen that resonance modes below 400 Hz are sensitive to USP stiffness changes. In our study, the stiffness values of both the RPs and USPs change with temperature, and a variation throughout the complete frequency domain is observed. As stated before, the f_{pin} mode remains relatively unchanged due to its lack of sensitivity to the stiffness of the pads. The variation of the global stiffness value is affected by the stiffnesses of the USP and RP. The loss factor increases so much that it suppresses the peaks of the resonances except for f_{pin}. Moreover, f_{in} can be determined based on the ballast receptance functions. If two f_{in} are compared, the one in Track B is not shifted as substantially that in Track A is, indicating that the bridge's contribution to the global mass is greater than its contribution to stiffness. Finally, it is concluded that the amplitude of the f_{in} receptance function can vary 8–10 times larger considering the responses of the resilient elements under different temperatures. Variations in ballast stiffness with temperature are not studied in this paper.

4 Conclusion

In this paper, a mathematical model for the transition zone between an open ballasted track (Track A) and a bridge (Track B) is proposed. The governing equations are derived, and the VE forces of the pads are integrated into the equation system. To evaluate the dynamics of the sleeper, ballast, and USP together, a unit mass is placed between the USP and the ballast spring by keeping the system isolated from a singularity condition. The VE properties of the USP and RP, like the storage modulus and the loss factor, are obtained via DMA tests. The FDM parameters of the pads are fitted, and GMM coefficients are then calculated for a specified frequency range (0.01–5000 Hz). To implement VE forces in the railway superstructure model, a hybrid approach is proposed with the numerical solution scheme of hereditary integrals. To ensure the accuracy of semi-analytical modelling, FEM and field tests are performed, and a very good agreement is

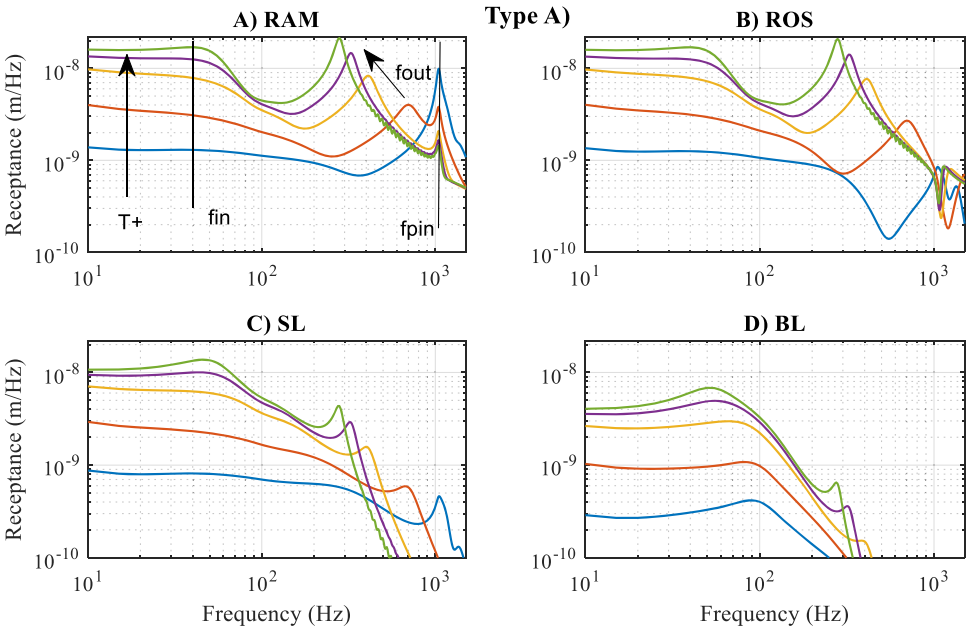


Fig. 21 Temperature effects on the receptance functions of Track A components

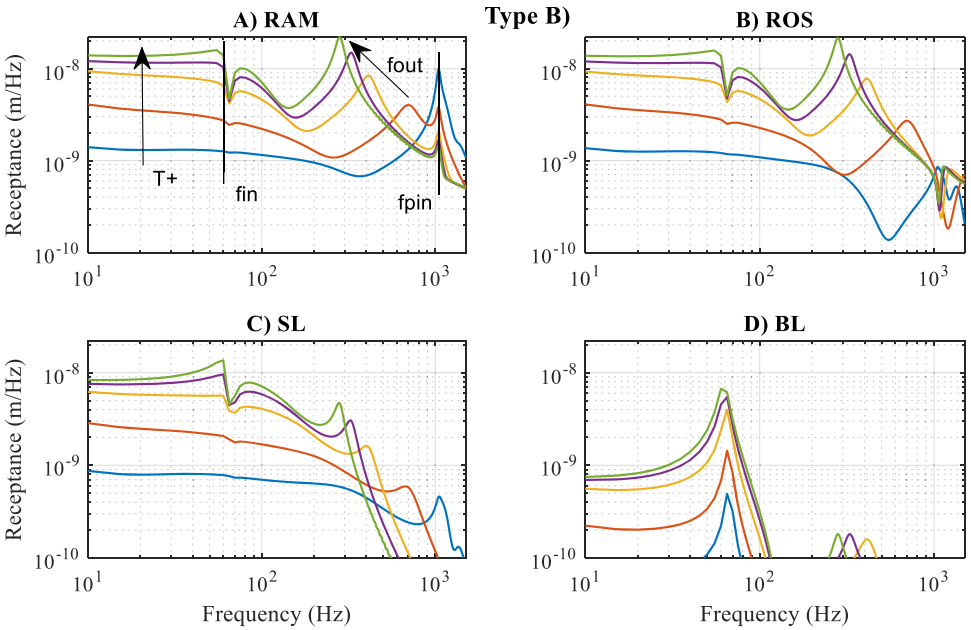


Fig. 22 Temperature effects on the receptance functions of Track B components

observed. Finally, receptance functions are plotted for investigating the frequency responses of the track elements. In this paper, appropriate modelling techniques developed for the mitigation of high-amplitude dynamic effects in railway crossing zones, time and frequency domain analyses, and field tests are carried out, the following conclusions are reached, and an important contribution to the literature in this field is presented.

- Unit mass integration to provide USP and ballast connection is successfully implemented by avoiding mathematical singularity. Therefore, the VE and elastic responses correspond to each other.
- The semi-analytical method clearly outperforms FEM in terms of computation time costs. FEM calculations take at least 50 times longer to make. In addition to field tests, the verification of parameters and the proposed method is also provided.
- Time domain analyses show that GMM is superior to KVM, especially in predicting accelerations in the sleeper and the ballast.

- The energy dissipation capacities between the pads are significantly clear. USP Type 2 has a significant advantage over USP Type 1 with a 2.73-fold difference.
- At different train speeds, the maximum values of the vertical accelerations of the ballast and USP forces are predicted.
- Temperature variations affect the stiffness-dependent resonance modes. Shifted loss factors also have peaks that are smoother or more visible.
- The out-of-phase resonance mode, f_{out}, is the most sensitive characteristic behaviour to temperature alteration.
- If frequency zones above 100 Hz are considered, GMM should be utilised to obtain more accurate results compared to KVM.
- In Track B, the bridge has a greater impact on the global mass than on the global stiffness.

The reasons for the significance of this study from an engineering point of view are:

- By taking into account the effects of temperature changes on the mechanical properties of the material, the presented approach allows for a more informed selection of USPs and RPs in all types of structures (transition zone, open track, and bridge). This allows a better isolation of vibration and noise from low to high frequencies.
- Since the effect of temperature variability is considered in material modelling, the current framework can be extended to the production of special elastomer pads with optimal stiffness for noise and vibration isolation in regions with high temperature variability.
- Due to the sudden change in the superstructure in transition zones, voids are formed under the sleeper over time. Again, by modelling that accounts for the change in the mechanical properties of the material with temperature, the impact is reduced, void formation times are prolonged, and maintenance costs are lowered.

According to the points presented above, the proposed method is a robust tool for examining the dynamic behaviours of USPs, sleepers, and ballasts for transition zones. The optimisation of the railway superstructure could be studied more precisely by taking these into consideration. For instance, the geometric and material properties of the resilient elements, as well as the design parameters of the ballast, sleeper, and rail, can be determined according to temperature changes in future studies.

Author Contributions Arif Ulu and Aytac Arikoglu were responsible for conceptualization, methodology, software, and writing—original draft. Muzaffer Metin contributed to conceptualization, administration, funding, and writing—original draft. Ozgur Demir took part in conceptualization, methodology, FEM, and writing—original draft.

Funding Open access funding provided by the Scientific and Technological Research Council of Türkiye (TÜBİTAK). The authors would like to thank TCDD-DATEM (Türkiye State Railways-Research and Technology Center) for providing field measurement results and basic FEM geometry. The authors would also like to thank the Faculty of Aeronautics and Astronautics at Istanbul Technical University for making their laboratories available.

Declarations

Conflict of interest The authors declare that they have no known competing financial interests or personal relationships that could have appeared to influence the work reported in this paper.

Open Access This article is licensed under a Creative Commons Attribution 4.0 International License, which permits use, sharing, adaptation, distribution and reproduction in any medium or format, as long as you give appropriate credit to the original author(s) and the source, provide a link to the Creative Commons licence, and indicate if changes were made. The images or other third party material in this article are included in the article's Creative Commons licence, unless indicated otherwise in a credit line to the material. If material is not included in the article's Creative Commons licence and your intended use is not permitted by statutory regulation or exceeds the permitted use, you will need to obtain permission directly from the copyright holder. To view a copy of this licence, visit http://creativecommons.org/licenses/by/4.0/.

Appendix A

See Appendix Tables 4, 5, 6, and 7.

Table 4 Parameters obtained for ten-parameter FDM with shift factors

	Parameters	RP	USP Type 1	USP Type 2
Fractional derivative model @0 °C	E_∞ (MPa)	14.2008	0.6247	3.7931
	Ω	193.4254	787.9164	107.4292
	α	0.2441	0.3789	0.2688
	β	0.0514	0.1144	0.1905
	γ	0.3124	0.2261	0.1441
	φ	0.0139	0.0143	0.0014
	λ_1 (MPa)	420.5019	32.0732	52.0241
	λ_3	0.6364	0.4703	0.4633
	λ_3	110.4063	17.8038	74.3012
	τ_{FD} (s)	− 6.118	4.2085	0.3384
log a_T	$T = -30$ °C	3.7772	5.7200	5.3271
	$T = -20$ °C	2.3610	3.6928	3.5183
	$T = -10$ °C	1.0815	1.7405	1.7728
	$T = 0$ °C	0	0	0
	$T = 10$ °C	− 1.1339	− 1.8444	− 1.6552
	$T = 20$ °C	− 2.0057	− 3.4193	− 3.0376
	$T = 30$ °C	− 2.7278	− 4.8155	− 4.0417
	$T = 40$ °C	− 3.4305	− 6.0198	− 5.0185
	$T = 50$ °C	− 4.4124	− 7.0356	− 7.2223

Table 5 GMM parameters obtained for RP

	Unit	− 30 °C	− 20 °C	− 10 °C	0 °C	10 °C	20 °C	30 °C	40 °C	50 °C
E_∞	MPa	34.4764	25.7578	21.1776	18.2834	16.5317	15.6152	15.1215	14.7851	14.5068
E_1		164.6865	167.7246	111.5342	59.7717	31.6727	18.2817	11.9670	8.2280	5.4033
E_2		145.5934	97.9992	49.1361	23.3454	12.1409	7.4697	5.3114	4.0480	2.9579
E_3		123.0803	60.8153	27.5958	13.2288	7.3666	4.9709	3.8243	3.0570	2.2785
E_4		77.3256	32.4572	14.4451	7.4016	4.6121	3.4533	2.8042	2.2694	1.5463
E_5		43.9234	17.3332	8.1827	4.7603	3.3584	2.5748	2.0200	1.5188	0.9632
E_6		21.8741	9.3973	5.0454	3.3455	2.4397	1.8071	1.3473	0.9597	0.5573
E_7		15.0004	6.3995	3.9805	2.7753	1.9203	1.3023	0.8953	0.5988	0.3309
τ_1	s	0.0001	0.0001	0.0001	0.0001	0.0001	0.0001	0.0001	0.0001	0.0001
τ_2		0.001	0.001	0.001	0.001	0.001	0.001	0.001	0.001	0.001
τ_3		0.01	0.01	0.01	0.01	0.01	0.01	0.01	0.01	0.01
τ_4		0.1	0.1	0.1	0.1	0.1	0.1	0.1	0.1	0.1
τ_5		1	1	1	1	1	1	1	1	1
τ_6		10	10	10	10	10	10	10	10	10
τ_7		100	100	100	100	100	100	100	100	100

Table 6 GMM parameters obtained for USP Type 1

	Unit	− 30 °C	− 20 °C	− 10 °C	0 °C	10 °C	20 °C	30 °C	40 °C	50 °C
E_∞	MPa	218.4628	162.0003	117.0000	72.6573	42.1070	22.5510	10.6877	5.0003	2.5912
E_1		38.2459	43.4496	45.0294	39.9384	34.8871	31.1202	28.8001	27.0391	24.0625
E_2		32.9919	35.2628	34.0953	29.2025	25.4521	23.2049	21.4699	19.1457	15.7776
E_3		35.9691	36.2042	33.4962	28.1149	24.9404	23.0241	20.2570	16.7992	13.2972
E_4		36.1327	34.3530	30.5087	25.7823	23.4115	20.9626	17.0219	13.2854	10.3473
E_5		35.8976	32.3733	28.3208	24.4412	22.1759	18.3968	13.8293	10.5754	7.8648
E_6		33.9084	29.4823	26.0754	22.9368	19.7989	14.9736	10.9001	8.0040	4.7298
E_7		36.8357	31.4634	28.0383	24.5180	19.0233	13.3811	9.1699	5.1761	2.5767
τ_1	s	0.0001	0.0001	0.0001	0.0001	0.0001	0.0001	0.0001	0.0001	0.0001
τ_2		0.001	0.001	0.001	0.001	0.001	0.001	0.001	0.001	0.001
τ_3		0.01	0.01	0.01	0.01	0.01	0.01	0.01	0.01	0.01
τ_4		0.1	0.1	0.1	0.1	0.1	0.1	0.1	0.1	0.1
τ_5		1	1	1	1	1	1	1	1	1
τ_6		10	10	10	10	10	10	10	10	10
τ_7		100	100	100	100	100	100	100	100	100

Table 7 GMM parameters obtained for USP Type 2

	Unit	− 30 °C	− 20 °C	− 10 °C	0 °C	10 °C	20 °C	30 °C	40 °C	50 °C
E_∞	MPa	86.0070	58.4923	38.8606	25.0902	16.5832	11.9717	9.6700	8.0332	5.8250
E_1		59.7662	52.3302	38.6274	27.3197	20.7234	16.4040	13.8731	11.3833	6.7372
E_2		45.7115	34.9320	24.5733	17.8679	13.5477	10.7084	8.6989	7.0386	4.0135
E_3		41.8562	29.9117	21.3363	15.8985	12.0926	9.2288	7.3498	5.7548	3.0858
E_4		34.7881	24.2248	17.7294	13.3613	9.8165	7.2340	5.6410	4.3332	2.2760
E_5		28.5853	20.2310	15.2228	11.2515	8.0034	5.7151	4.3411	3.2709	1.7116
E_6		23.1280	16.9690	12.7616	9.1285	6.2098	4.2737	3.2081	2.3731	1.1175
E_7		22.0789	16.4058	12.0404	8.2510	5.3766	3.6292	2.6652	1.9623	0.9901
τ_1	s	0.0001	0.0001	0.0001	0.0001	0.0001	0.0001	0.0001	0.0001	0.0001
τ_2		0.001	0.001	0.001	0.001	0.001	0.001	0.001	0.001	0.001
τ_3		0.01	0.01	0.01	0.01	0.01	0.01	0.01	0.01	0.01
τ_4		0.1	0.1	0.1	0.1	0.1	0.1	0.1	0.1	0.1
τ_5		1	1	1	1	1	1	1	1	1
τ_6		10	10	10	10	10	10	10	10	10
τ_7		100	100	100	100	100	100	100	100	100

Appendix B

Time-dependent vectors of global matrices:

$$q_R = \{T_1 R_1 \cdots T_n R_n\}^T_{2nx1}$$
$$W_S = \left\{w_{s,1} \cdots w_{s,n_p}\right\}^T_{n_p x1}$$
$$W_U = \left\{w_{u,1} \cdots w_{u,n_p}\right\}^T_{n_p x1}$$
$$W_B = \left\{w_{b,1} \cdots w_{b,n_{p1}}\right\}^T_{n_{p1} x1}$$

$$q_{\mathrm{BR}} = \left\{T_{\mathrm{br},1} \cdots T_{\mathrm{br},n_{\mathrm{br}}}\right\}^T_{n_{\mathrm{br}} x1} \tag{B.1}$$

Submatrices of the global mass matrix:

$$\mathbf{M_R} = \begin{bmatrix} \frac{\rho AL}{2} & \cdots & 0 \\ \vdots & \ddots & \vdots \\ 0 & \cdots & \frac{\rho IL}{2} \end{bmatrix}_{2nx2n} \qquad \mathbf{M_S} = \begin{bmatrix} m_s & \cdots & 0 \\ \vdots & \ddots & \vdots \\ 0 & \cdots & m_s \end{bmatrix}_{n_p x n_p}$$

$$\mathbf{M}_{\mathrm{U}} = \begin{bmatrix} m_u & \cdots & 0 \\ \vdots & \ddots & \vdots \\ 0 & \cdots & m_u \end{bmatrix}_{n_p x n_p} \quad \mathbf{M}_{\mathrm{B}} = \begin{bmatrix} m_b & \cdots & 0 \\ \vdots & \ddots & \vdots \\ 0 & \cdots & m_b \end{bmatrix}_{n_{p1} x n_{p1}}$$

$$\mathbf{M}_{\mathrm{BR}} = \begin{bmatrix} \frac{m_{\mathrm{br}} L_{\mathrm{br}}}{2} & \cdots & 0 \\ \vdots & \ddots & \vdots \\ 0 & \cdots & \frac{m_{\mathrm{br}} L_{\mathrm{br}}}{2} \end{bmatrix}_{n_{\mathrm{br}} x n_{\mathrm{br}}} \tag{B.2}$$

$\mathbf{K}_{\mathrm{R}}$ is the rail stiffness matrix:

$$\mathbf{K}_{\mathrm{R}} = \begin{bmatrix} \frac{\kappa AGL}{2}\left(\frac{\pi}{L}\right)^2 & \cdots & 0 \\ \vdots & \ddots & \vdots \\ 0 & \cdots & \frac{EIL}{2}\left(\frac{n\pi}{L}\right)^2 + \frac{\kappa AGL}{2} \end{bmatrix}_{2nx2n} \tag{B.3}$$

$\mathbf{K}_{\mathrm{B}}$ is the ballast stiffness matrix:

$$\mathbf{K}_{\mathrm{B}} = \begin{bmatrix} k_b & & \\ & \ddots & \\ & & k_b \end{bmatrix}_{n_p x n_p} \tag{B.4}$$

$\mathbf{K}_{\mathrm{BFW}}$ is the ballast interaction stiffness matrix of Type A zone:

$$\mathbf{K}_{\mathrm{BFW}} = [\mathbf{K}_{\mathrm{BFW1}}]_{n_{p1} x n_{p1}}$$

$$\mathbf{K}_{\mathrm{BFW1}} = \begin{bmatrix} k_b + k_{f,1} + 2k_w & -k_w & \cdots & 0 \\ -k_w & \ddots & \ddots & \vdots \\ \vdots & \ddots & \ddots & -k_w \\ 0 & \cdots & -k_w & k_b + k_{f,n_{p1}} + 2k_w \end{bmatrix}_{n_{p1} x n_{p1}} \tag{B.5}$$

$\mathbf{K}_{\mathrm{BR}}$ is the bridge stiffness matrix:

$$\mathbf{K}_{\mathrm{BR}} = \begin{bmatrix} \left(\frac{\pi}{L_{br}}\right)^4 & \cdots & 0 \\ \vdots & \ddots & \vdots \\ 0 & \cdots & \left(\frac{n_{br}\pi}{L_{br}}\right)^4 \end{bmatrix}_{n_{br} x n_{br}} \tag{B.6}$$

$\mathbf{K}_{\mathrm{FBR}}$ is the ballast–bridge interaction stiffness matrix:

$$\mathbf{K}_{\mathrm{FBR}} = \begin{bmatrix} \mathbf{K}_{\mathrm{FBR1}} & \mathbf{K}_{\mathrm{FBR2}} \end{bmatrix}_{n_{br} x n_p} \tag{B.7}$$

$$\mathbf{K}_{\mathrm{FBR1}} = [0]_{n_{br} x n_{p1}} \tag{B.8}$$

$$\mathbf{K}_{\mathrm{FBR2}} = -\begin{bmatrix} \left(k_{b,n_{p1}+1} + 2k_w\right)\phi_{\mathrm{br},1}\left(L_{p\mathrm{br},1}\right) & \cdots & \left(k_{b,n_p} + 2k_w\right)\phi_{br,1}\left(L_{p\mathrm{br},n_{p2}}\right) \\ \vdots & \ddots & \vdots \\ \left(k_{b,n_{p1}+1} + 2k_w\right)\phi_{\mathrm{br},n_{\mathrm{br}}}\left(L_{p\mathrm{br},1}\right) & \cdots & \left(k_{b,n_p} + 2k_w\right)\phi_{\mathrm{br},n_{\mathrm{br}}}\left(L_{p\mathrm{br},n_{p2}}\right) \end{bmatrix}_{n_{\mathrm{br}} x n_{p2}} \tag{B.9}$$

$\mathbf{K}_{\mathrm{BRF}}$ is the bridge–ballast interaction stiffness matrix:

$$\mathbf{K}_{\mathrm{BRF}} = \sum_{k=1}^{n_{p2}} \left(k_{b,n_{p1}+k} + 2k_w\right) \begin{bmatrix} \phi_{\mathrm{br},1}\left(L_{p\mathrm{br},k}\right)\phi_{\mathrm{br},1}\left(L_{p\mathrm{br},k}\right) & \cdots & \phi_{\mathrm{br},n_{\mathrm{br}}}\left(L_{p\mathrm{br},k}\right)\phi_{\mathrm{br},1}\left(L_{p\mathrm{br},k}\right) \\ \vdots & \ddots & \vdots \\ \phi_{\mathrm{br},1}\left(L_{p\mathrm{br},k}\right)\phi_{\mathrm{br},n_{\mathrm{br}}}\left(L_{p\mathrm{br},k}\right) & \cdots & \phi_{\mathrm{br},n_{\mathrm{br}}}\left(L_{p\mathrm{br},k}\right)\phi_{\mathrm{br},n_{\mathrm{br}}}\left(L_{p\mathrm{br},k}\right) \end{bmatrix}_{n_{\mathrm{br}} x n_{\mathrm{br}}} \tag{B.10}$$

P_V is the moving wheel forces of the train:

$$\{P_V\}_{2nx1} = \left\{P_{V1} + ... + P_{Vn_v}\right\} = P_1 \begin{Bmatrix} \phi_i\left(vt - L_{v,1}\right) \\ 0 \\ \vdots \\ \phi_n\left(vt - L_{v,1}\right) \\ 0 \end{Bmatrix} + ... + P_{n_v} \begin{Bmatrix} \phi_i\left(vt - L_{v,n_v}\right) \\ 0 \\ \vdots \\ \phi_n\left(vt - L_{v,n_v}\right) \\ 0 \end{Bmatrix} \tag{B.11}$$

$F_{\mathrm{PAD},\,R}$ is the rail pad forces acting on the rail:

$$\left\{F_{P\mathrm{AD},\,R}\right\}_{2nx1} = P_{\mathrm{pad},1} \begin{Bmatrix} \phi_i\left(L_{p,1}\right) \\ 0 \\ \vdots \\ \phi_n\left(L_{p,1}\right) \\ 0 \end{Bmatrix} + \ldots + P_{\mathrm{pad},n_p} \begin{Bmatrix} \phi_i\left(L_{p,n_p}\right) \\ 0 \\ \vdots \\ \phi_n\left(L_{p,n_p}\right) \\ 0 \end{Bmatrix} \tag{B.12}$$

$F_{R,\mathrm{PAD}}$ and F_{USP} are the RP forces acting on the sleepers and under sleeper forces acting on the RP and unit masses.

$$\left\{F_{R,\mathrm{PAD}}\right\}_{n_p x1} = \left\{P_{\mathrm{pad},1},\ \ldots,\ P_{\mathrm{pad},n_p}\right\}^T$$
$$\{F_{\mathrm{USP}}\}_{n_p x1} = \left\{P_{\mathrm{usp},1},\ \ldots,\ P_{\mathrm{usp},n_p}\right\}^T \tag{B.13}$$

References

1. Coelho, B.; Priest, J.; Holscher, P.; Powrie, W.: Monitoring of Transition Zones in Railways. Engineering Technics Press (2009)
2. Nasrollahi, K.; Nielsen, J.C.O.; Aggestam, E.; Dijkstra, J.; Ekh, M.: Prediction of long-term differential track settlement in a transition zone using an iterative approach. Eng. Struct. **283**, 115830 (2023)
3. Sañudo, R.; dell'Olio, L.; Casado, J.A.; Carrascal, I.A.; Diego, S.: Track transitions in railways: a review. Constr. Build. Mater. **112**, 140–157 (2016)
4. Ngamkhanong, C.; Nascimento, A.T.; Kaewunruen, S.: Economics of track resilience. In: IOP Conference Series: Materials Science and Engineering, vol. 471, p. 062040 (2019)
5. Real-Herráiz, J.; Zamorano-Martín, C.; Real-Herráiz, T.; Morales-Ivorra, S.: New transition wedge design composed by prefabricated reinforced concrete slabs. Latin Am. J. Solids Struct. **13**, 1431–1449 (2016)
6. Insa, R.; Salvador, P.; Inarejos, J.; Roda, A.: Analysis of the influence of under sleeper pads on the railway vehicle/track dynamic interaction in transition zones. Proc. Inst. Mech. Eng. Part F J. Rail Rapid Transit. **226**, 409–420 (2011)
7. Paixão, A.; Alves Ribeiro, C.; Pinto, N.; Fortunato, E.; Calçada, R.: On the use of under sleeper pads in transition zones at railway underpasses: experimental field testing. Struct. Infrastruct. Eng. **11**, 112–128 (2015)
8. Ngamkhanong, C.; Kaewunruen, S.: Effects of under sleeper pads on dynamic responses of railway prestressed concrete sleepers subjected to high intensity impact loads. Eng. Struct. **214**, 110604 (2020)
9. Ang, K.K.; Dai, J.: Response analysis of high-speed rail system accounting for abrupt change of foundation stiffness. J. Sound Vib. **332**, 2954–2970 (2013)
10. Johansson, A.; Nielsen, J.C.O.; Bolmsvik, R.; Karlström, A.; Lundén, R.: Under sleeper pads—influence on dynamic train—track interaction. Wear **265**, 1479–1487 (2008)
11. Nicks, J.E.: The Bump at the End of the Railway Bridge. Texas A&M University (2009)
12. Varandas, J.N.; Hölscher, P.; Silva, M.A.G.: Dynamic behaviour of railway tracks on transitions zones. Comput. Struct. **89**, 1468–1479 (2011)
13. Alves Ribeiro, C.; Paixão, A.; Fortunato, E.; Calçada, R.: Under sleeper pads in transition zones at railway underpasses: numerical modelling and experimental validation. Struct. Infrastruct. Eng. **11**, 1432–1449 (2015)
14. Schneider, P.; Bolmsvik, R.; Nielsen, J.C.O.: In situ performance of a ballasted railway track with under sleeper pads. Proc. Inst. Mech. Eng. Part F J. Rail Rapid Transit. **225**, 299–309 (2011)
15. Stark, T.D.; Wilk, S.T.: Root cause of differential movement at bridge transition zones. Proc. Inst. Mech. Eng. Part F J. Rail Rapid Transit. **230**, 1257–1269 (2016)
16. Aggestam, E.; Nielsen, J.C.O.: Multi-objective optimisation of transition zones between slab track and ballasted track using a genetic algorithm. J. Sound Vib. **446**, 91–112 (2019)
17. Çati, Y.; Gökçeli, S.; Anil, Ö.; Korkmaz, C.S.: Experimental and numerical investigation of usp for optimization of transition zone of railway. Eng. Struct. **209**, 109971 (2020)
18. Man, A.P.D.: Dynatrack: A Survey of Dynamic Railway Track Properties and Their Quality. DUP Science, Delft (2002)
19. Paixão, A.; Varandas, J.N.; Fortunato, E.; Calçada, R.: Numerical simulations to improve the use of under sleeper pads at transition zones to railway bridges. Eng. Struct. **164**, 169–182 (2018)
20. Huang, X.; Zeng, Z.; Wang, D.; Luo, X.; Li, P.; Wang, W.: Experimental study on the vibration reduction characteristics of the floating slab track for 160 km/h urban rail transit. Structures **51**, 1230–1244 (2023)
21. Hunt, H.E.M.; Winkler: settlement of railway track near bridge abutments. Proc. Inst. Civ. Eng. **123**, 68–73 (1997)
22. Mottahed, J.; Zakeri, J.A.; Mohammadzadeh, S.: Field and numerical investigation of the effect of under-sleeper pads on the dynamic behavior of railway bridges. Proc. Inst. Mech. Eng. Part F J. Rail Rapid Transit. **232**, 2126–2137 (2018)
23. Cui, X.-H.; Xiao, H.; Ling, X.: Analysis of ballast breakage in ballast bed when using under sleeper pads. Geomech. Geoeng. **17**, 677–688 (2022)
24. Myskowski, B.; Lima, A.D.O.; Edwards, J.R.: Under tie (sleeper) pads—a state of the art review. Constr. Build. Mater. **383**, 131239 (2023)

25. Chi, Y.; Xiao, H.; Zhang, Z.; Wang, Y.: Field experiment and numerical simulation investigation on the mechanical properties of ballast bed with elastic sleepers. Constr. Build. Mater. **397**, 132361 (2023)
26. Mayuranga, H.G.S.; Navaratnarajah, S.K.; Bandara, C.S.; Jayasinghe, J.A.S.C.: Elastic inclusions in ballasted tracks—a review and recommendations. Int. J. Rail Transp.1–28 (2023)
27. Arikoglu, A.: A new fractional derivative model for linearly viscoelastic materials and parameter identification via genetic algorithms. Rheol. Acta **53**, 219–233 (2014)
28. Ulu, A.; Arikoglu, A.; Metin, M.; Demir, O.: A novel viscoelastic modelling of railway track elements and experimental validation. Constr. Build. Mater. **356**, 129235 (2022)
29. Canga Ruiz, A.E.; Qian, Y.; Edwards, J.R.; Dersch, M.S.: Analysis of the temperature effect on concrete crosstie flexural behavior. Constr. Build. Mater. **196**, 362–374 (2019)
30. Metin, M.; Ulu, A.; Demir, O.; Arikoglu, A.: Dynamic analysis of railway with locally continuous supported superstructures. Eng. Comput. **36**, 3047–3069 (2019)
31. Paixão, A.; Fortunato, E.; Calçada, R.: Transition zones to railway bridges: track measurements and numerical modelling. Eng. Struct. **80**, 435–443 (2014)
32. Zhu, Z.; Qin, Y.; Wang, K.; Gong, W.; Zheng, W.: Determination of settlement limit values for a new concrete box subgrade with ballasted track. Structures **45**, 1646–1656 (2022)
33. Kouroussis, G.; Connolly, D.P.; Verlinden, O.: Railway-induced ground vibrations—a review of vehicle effects. Int. J. Rail Transp. **2**, 69–110 (2014)
34. Blanco, B.; Alonso, A.; Kari, L.; Gil-Negrete, N.; Giménez, J.G.: Distributed support modelling for vertical track dynamic analysis. Veh. Syst. Dyn. **56**, 529–552 (2018)